Plutonic xenoliths reveal the influence of cryptic melt-mush reaction processes in the plumbing system beneath St Vincent, Lesser Antilles arc

Joshua R. Brown[1,2*], George F. Cooper[3], Madeleine C.S. Humphreys[1], Alexander A. Iveson[4], Christopher J. Ottley[1], Julie Prytulak[1,5]

[1]Department of Earth Sciences, Durham University, Durham, DH1 3LE, UK

[2]School of Natural Sciences, Trinity College Dublin, Dublin 2, Dublin, Ireland

[3]School of Earth and Environmental Sciences, Cardiff University, Cardiff, CF10 3AT, UK

[4]Pacific Northwest National Laboratory, Richland, WA 99352, United States of America

[5]Department of Earth, Ocean and Atmospheric Sciences, The University of British Columbia, Vancouver, Canada, V6T 1Z4

*corresponding author E-mail: jbrown4@tcd.ie

Running title: Plutonic xenoliths reveal magmatic processes

ABSTRACT

In subduction zones, it is widely established that magmas are stored as crystal dominated mush within sub-volcanic plumbing systems. In these mush-dominated systems, it is likely that melt-mush reactions between migrating melts and the pre-existing mush influence the chemical evolution of magmas. However, melt-mush reactions and their effect on the chemical evolution of arc magmas can be elusive and cannot be constrained when studying erupted lavas in isolation. In this study, we focus on the island of St. Vincent in the Lesser Antilles volcanic arc because (1) the composition of erupted lavas has been interpreted to reflect simple fractional crystallisation, with minimal influence of other magmatic processes, and (2) an abundance of plutonic xenoliths (erupted fragments of crystal mush) can be found within the eruptive products. Thus, we are able to compare interpretations gleaned from the chemistry of erupted lavas with new observations of the crystal mush in the same magmatic system. To this end, textural analyses were undertaken on seventeen representative plutonic xenoliths from St Vincent, and four of these samples (two olivine gabbros, two hornblende-olivine gabbros) were studied in detail via element mapping, mineral trace element analyses and geochemical modelling. The chemical, textural and mineralogical characteristics of the olivine gabbros were best explained via fractional crystallisation in the mid-upper crust (~6-18 km depth). However, the hornblende-olivine gabbros (two of seventeen samples studied) contained clear textural evidence for melt-mush reaction in the mid-upper crust. The trace element compositions of minerals such as clinopyroxene in these two samples were best reproduced via assimilation-fractional crystallisation modelling, simulating melt-mush reactions, supporting the textural evidence. Our plutonic xenoliths reveal that in addition to fractional crystallisation, cryptic (i.e. not directly recorded in lavas) melt-mush reaction processes also contribute to magma chemical evolution, particularly influencing trace elements, within the sub-volcanic plumbing system. Textural evidence for melt-mush reaction is increasingly reported in plutonic xenoliths from other active arcs and exhumed arc crustal sections, suggesting that this process is ubiquitous in mush-dominated arc plumbing systems. Melt-mush reaction therefore represents an important process contributing to arc magma and arc crust trace element chemical diversity.

Keywords: geochemistry; igneous petrology; magmatic plumbing systems; melt-mush reaction; fractional crystallisation; subduction zone magmatism

INTRODUCTION

A growing body of evidence supports the idea that lavas erupted at arc volcanoes are derived from magmatic plumbing systems within which magma is predominantly stored as crystal dominated mush, rather than melt dominated magma chambers (Bachmann & Bergantz, 2004; Cashman *et al*., 2017: Bachmann & Huber, 2019; Edmonds *et al*., 2019; Sparks *et al*., 2019; Paulatto *et al*., 2022). Mush is defined as "a supersolidus rock with a largely interconnected melt phase within a continuous crystal framework" (Humphreys *et al*., 2025). Within mush dominated plumbing systems, a plethora of processes that modify primary magma compositions take place, including fractional crystallisation, melt-rock and melt-mush reaction, wallrock/crustal assimilation and mixing (Hildreth & Moorbath, 1988; Davidson *et al*., 2005; Turner & Langmuir 2015, 2022; Marxer *et al*., 2022; Cooper *et al*., 2016; Klaver *et al*., 2017; Boulanger & France, 2023). It is difficult to directly investigate magmatic processes in crystal mush dominated plumbing systems using erupted lavas, because their chemistry represents the time-integrated result of multiple processes that have operated throughout their journey from initial mantle partial melting to eruption at the surface (e.g. Davidson *et al*., 2007). Instead, plutonic xenoliths, carried to the surface in erupted lavas, offer an alternative, more direct means of interrogating the processes occurring within crystal mushes. Plutonic xenoliths are interpreted to represent fragments of mush derived from a range of depths (Chadwick *et al*., 2013; Stamper *et al*., 2014; Cooper *et al*., 2016; 2019; Price *et al*., 2016; Melekhova *et al*., 2017; 2019; Camejo-Harry *et al*., 2018). These samples allow detailed observation of the spatial relationships between the mineral phases and interstitial melt within the mush. Such textural observations provide key information on magmatic processes that cannot be obtained from the chemical compositions of lavas alone, or the compositions and textures of free crystals carried in lavas.

Although the ubiquity of mush beneath active arc volcanoes is generally accepted, its impact on magma chemical evolution and the compositions of erupted lavas is less certain. A consequence of mush-dominated plumbing systems is the idea that the reaction of migrating melts with a pre-existing crystal mush framework (often termed “reactive melt flow” or “melt-mush reaction”) is a primary process in the chemical evolution of magmas, in addition to crystallisation driven differentiation (Lissenberg & MacLeod, 2016; Jackson *et al*., 2018; Lissenberg *et al.*, 2019; Blundy, 2022; Boulanger & France, 2023; Li *et al*., 2024). In this study, we refer to interactions between melts and crystal mushes using the term “melt-mush reaction”. Evidence for melt-mush reaction has been largely based on textural features such as ragged or embayed crystal boundaries or cores, indicative of dissolution, and reaction-relationships between mineral phases (Smith, 2014; Cooper *et al*., 2016; Lissenberg & MacLeod, 2016; Melekhova *et al*., 2017; Sanfillipo *et al*., 2020; Boulanger *et al*., 2021). Textural indicators of melt-mush reaction have been identified in plutonic xenoliths and equivalent plutonic rocks from active and exhumed arcs (Costa *et al*., 2002; Smith, 2014; Bouilhol *et al*., 2015; Cooper *et al*., 2016; Klaver *et al*., 2017; Melekhova *et al*., 2017; Camejo-Harry *et al*., 2018; Villares *et al*., 2022), mid-ocean ridge (MOR) settings (Lissenberg *et al*., 2013; Lissenberg & MacLeod, 2016; Sanfillipo *et al*., 2020; Zhang *et al*., 2020; Boulanger *et al*., 2020, 2021; Ferrando *et al*., 2021; Boulanger & France, 2023), and ocean island volcanoes (Gleeson *et al*., 2020). Crystals and/or crystal zones that form during melt-mush reaction may also be identified through their distinctive enrichments in incompatible trace elements compared with crystal compositions produced by fractional crystallisation (Lissenberg & MacLeod, 2016; SanFillipo *et al*., 2020; Gleeson *et al*., 2020; Boulanger *et al*., 2021; Boulanger & France, 2023).

Plutonic xenoliths are abundant in volcanic deposits of the Lesser Antilles arc (LAA), including the active volcanic island of St Vincent. The (whole-rock) major and trace element compositions of erupted lavas on St. Vincent have been interpreted to reflect fractional crystallisation (Heath *et al*., 1998; Cole *et al*., 2019; Fedele *et al*., 2021) over a range of depths (Melekhova *et al*., 2015; 2019). Other crustal level processes such as country rock assimilation and magma mixing, which have potential to complicate interpretation of mush processes, have been shown to have negligible influence on St Vincent magma compositions (Heath *et al*., 1998; Tollan *et al*., 2012; Cole *et al*., 2019). In this study, we combine textural observations, chemical mapping and mineral trace element compositions to assess the record of crystallisation differentiation and melt-mush reaction processes in a suite of plutonic xenoliths from St Vincent. We show that in addition to fractional crystallisation, the plutonic xenoliths reveal cryptic melt-mush reaction processes operating in the mushy plumbing system which are obscured in the lavas. These processes have major implications for understanding the evolution of subduction zone magmas and influence the diversity of magma trace element compositions and the chemical heterogeneity of arc crust formed at subduction zones.

PLUTONIC XENOLITH SAMPLES

The plutonic xenoliths used in this study were collected in 2019 from St. Vincent. The majority (of 43 xenoliths) were collected *in situ* from lavas or pyroclastic density current deposits on the flanks of La Soufrière volcano and coastal exposures on the eastern side of the island. Together with previous work, the plutonic xenolith collection from St. Vincent is now exceptionally large at about 140 samples. Seventeen xenoliths were selected as representative from the newly collected sample suite and initially assessed via optical petrology of 17 thin sections covering macroscopically identifiable textural diversity (Supplementary Table ST1). Using the classification scheme of Streckeisen (1976), the plutonic xenolith suite includes troctolites (5 samples), olivine gabbros (6 samples), hornblende-olivine gabbros (2 samples), hornblende gabbros (1 sample) and gabbronorites (3 samples). Adcumulate textures (no interstitial melt or intercumulus mineral phases) are observed in olivine gabbros and gabbronorites. Troctolites and some olivine gabbros are characterised by the presence of interstitial glass lining crystal boundaries or as small pockets. Clinopyroxene forms a primocryst phase in olivine gabbros, gabbronorites and hornblende-olivine gabbros and occurs as an interstitial phase in two olivine gabbros. Interstitial amphibole in hornblende-olivine gabbros is texturally associated with and replaces the rims of clinopyroxene and/or olivine, whereas amphibole in the hornblende gabbro appears euhedral (crystal shapes partially obscured by alteration). Here, we focus on samples containing clinopyroxene and/or amphibole due to their variable textural relationships with other phases. Following our textural assessment of the 17 xenoliths (Supplementary Table ST1), we selected four texturally distinctive plutonic xenoliths for a detailed textural and elemental study (Table 1) to assess the record of crystallisation differentiation and melt-mush reaction processes.

ANALYTICAL METHODS

The compositions of mineral phases were determined via chemical mapping of whole thin sections and laser ablation inductively coupled plasma mass spectrometry (LA-ICP-MS). These methods are summarised here. Further details can be found in Supplementary File 1.

Thin Section Mapping

Chemical maps of whole thin sections were acquired via Energy Dispersive X-ray Spectroscopy (EDS), using a Zeiss Sigma HD field emission gun (FEG) SEM with two 150 mm^2 Oxford Instruments X-Max energy dispersive silicon drift detectors at Cardiff University. Prior to analysis, the thin sections were coated with a conductive layer (~ 20 nm) of carbon. The maps were acquired using an accelerating voltage of 20 kV, aperture size 120 µm and working distance of 8.9 mm. The magnification was adjusted depending on the typical crystal size in thin section, resulting in a pixel size of 22-24 µm. Pixel dwell time was set at 20 ms for all sample maps. Raw data were background corrected using Oxford Instruments AZtec software prior to generation of quantitative element maps.

The python GUI program "QUACK", developed at Cardiff University (Loocke, 2016), was used to process the background-corrected x-ray element maps generated in AZtec and produce maps of both the distribution of mineral phases and quantitative molar element ratios (plagioclase An, pyroxene and amphibole Mg#, olivine Fo). The software is available to download at https://mloocke.wixsite.com/qacd-quack, and full details regarding software development and testing via analysis of secondary standards are documented in Loocke (2016) (accessible online at https://orca.cardiff.ac.uk/id/eprint/97663/).

The phase distribution maps were used to calculate the mineral modal abundances, as area percentages, for each sample using the algorithms in the QUACK software. Plagioclase An, olivine Fo and pyroxene Mg# were quantified using the mineral specific regression equations (see Loocke, 2016 for full details). Amphibole Mg# was quantified using the general Mg# regression equation. Data quality of molar element ratio maps processed via QUACK was rigorously tested by Loocke (2016), via analysis of plagioclase, clinopyroxene and olivine standards with known An, Mg# and Fo. Percentage error on molar ratio measurements (deviation of mean measured value from accepted value of standard, expressed as a percentage) was determined as 0.20 % for plagioclase An, 0.59 % for clinopyroxene Mg# and 0.22 % for olivine Fo. The quantitative molar ratio maps in this study were acquired using the same SEM at Cardiff University (as Loocke, 2016) using near identical run conditions, therefore we infer that uncertainties on our molar ratio measurements are < 1%.

Sanfillipo et al. (2020) and Cooper et al. (2025) also used QUACK to quantify element maps of plutonic rock samples obtained at Cardiff University. These studies provide further evidence for the accuracy of this method. Plagioclase and diopside secondary standards analysed alongside samples by Cooper et al. (2025) were accurate to within 1.7% An, with a precision of ± 2.57 2SD, and accurate to within 0.4% Mg#, with a precision of ±0.25 2SD, respectively. Sanfillipo et al. (2020) showed that An, Mg# and Fo values derived from their quantified element maps differed from values derived from Electron Microprobe spot analyses of the same crystals by < 2 %.

LA-ICP-MS analyses

The trace element compositions of clinopyroxene and amphibole were analysed by laser ablation inductively coupled plasma mass spectrometry (LA-ICP-MS), using a Teledyne Analyte Excite Laser Ablation System coupled to a Thermo-Scientific X-Series 2 ICP-MS at Durham University. The laser was run with a fluence of 8.09 J/cm^2, a repetition rate of 8 Hz, and a 75 µm square spot size. Helium was used as the carrier gas (flow rate ~1 L min^{-1}), with Ar mixed in (~1 L min^{-1}) prior to the introduction of the sample into the mass spectrometer. We analysed NIST SRM 612 glass (Jochum *et al*., 2011) as the calibration standard and USGS standard reference material BCR-2G as a secondary standard. Each batch of analyses consisted of 16-20 ablations, with standard analyses bracketing the clinopyroxene/amphibole analyses. For each individual analysis, 30 s of gas blank was measured followed by 40 s ablation of standard/target crystal. Data reduction was carried out using the software Iolite (Paton *et al*., 2011). The internal standard was Ca (wt %) – a constant value of 16 wt % Ca was used for clinopyroxene and 8.6 wt % Ca for amphibole, due to the minimal variation in CaO in plutonic xenolith clinopyroxene (CaO = 20.5-23.5 wt %) and amphibole (CaO = 11.2-

12.3 wt %, see Supplementary File 1 for details). Repeat measurements of BCR-2G (n=32) showed that trace elements were measured within 15 % of preferred values (from the GeoREM database, Jochum *et al*., 2005, Supplementary Table ST3). Uncertainties on trace element data are provided both as internal 2SE (calculated by Iolite, shown in Supplementary Table ST2) and 2SD % (reproducibility). All 2SD % (calculated as 2SD/mean * 100) uncertainties, based on the reproducibility of measurements of BCR-2G (n=32), are less than 15 % relative, excluding Ti (22 %), Cr (16 %) and Lu (23 %) (Supplementary Table ST3).

RESULTS

Petrography

Olivine gabbro

The mineral assemblage consists of plagioclase (69 %) and olivine (22 %) as primocryst phases with crystal size varying from 0.5-5 mm, with interstitial clinopyroxene (8 %) and minor magnetite (1 %). The crystallisation sequence is olivine - plagioclase - clinopyroxene - magnetite. The sample has a mesocumulate texture with films of glass lining most crystal boundaries (Figure 1a, Supplementary Figure S1). Close to the contact with the host lava, interstitial glass between crystals is slightly more abundant and appears interconnected with the surrounding glass (Supplementary Figure S1), suggesting that the host lava partially infiltrated the xenolith. However, the interstitial glass towards the interior of the xenolith may either be an infiltrated melt from the host or trapped melt which has quenched. In some parts of the sample, crystals separated by interstitial melt have a “jigsaw fit” appearance (Supplementary Figure S1), suggesting that the melt has pushed the crystals apart from each other.

Ol-Cpx gabbro

The mineral assemblage consists of plagioclase (52 %), olivine (23 %) and clinopyroxene (25 %) as primocryst phases (Figure 1b), with crystal size varying from 0.5-3 mm. The crystallisation sequence is olivine - plagioclase - clinopyroxene. The sample has an adcumulate texture (no interstitial melt) and well equilibrated, 120° crystal boundaries between the three primocryst phases are common (Supplementary Figure S1).

Banded gabbro

The mineral assemblage consists of plagioclase (58 %), olivine (2 %), and clinopyroxene (29 %) as primocryst phases, plus interstitial amphibole (7 %) and magnetite (4 %), with crystal size varying from 0.2-3 mm. A key feature is the presence of a texturally and mineralogically distinct band, approximately 1 cm wide (Supplementary Figure S2). In thin section, the band is characterized by a generally smaller crystal size, melt and fluid inclusion rich plagioclase cores and clear rims and the absence of olivine (Figure 2a,d,e). This feature is hereon referred to as the "plag-cpx band". The remainder of the sample outside the band is referred to as the sample "matrix" (Figure 2a). The matrix lacks interstitial glass. Well equilibrated contacts between (inclusion free) plagioclase and olivine (and some clinopyroxene) primocrysts are common (Supplementary Figure S2). Some matrix clinopyroxene display more irregular crystal shapes, indicative of additional intercumulus growth. Amphibole is distributed in patches within the sample matrix and notably only occurs outside the plag-cpx band. Amphibole is generally anhedral and typically found associated with and overgrowing the rims of clinopyroxene (Figure 2b,c) and occasionally, olivine.

Poikilitic gabbro

The mineral assemblage consists of plagioclase (53 %), olivine (8 %), clinopyroxene (12 %), orthopyroxene (12 %), and amphibole (15 %) with minor interstitial apatite, oxides and very rare sulfides. Crystal size varies from 0.3-4 mm, with many crystals (particularly plagioclase) measuring < 1mm. Two clinopyroxene size populations (> 1 mm euhedral, < 1 mm subhedral) are present. A key feature is the presence of poikilitic amphibole throughout the sample, which replaces the embayed/rounded rims of clinopyroxene and/or olivine (Figure 3a,b,d, Supplementary Figure S1). In several areas of the thin section, the poikilitic amphibole contain < 1 mm plagioclase inclusions, which do not show embayed crystal boundary junctions with the amphibole (Supplementary Figure S1), unlike the contacts between amphibole and clinopyroxene, suggesting that some plagioclase co-crystallised with the amphibole. Olivine is commonly altered to iddingsite. Where olivine is not enclosed by amphibole, it is typically rounded/embayed and enclosed by orthopyroxene (Figure 3c). Plagioclase exhibits a wide range of zoning patterns with some crystals displaying complex oscillatory zonation and relict/patchy cores (Figure 3e).

Mineral major element compositions

The compositional ranges (molar element ratios An, Mg#, Fo) of the main mineral phases in each plutonic xenolith sample are listed in Table 1 and illustrated in Supplementary Figure S3. In the olivine gabbro, olivine displays a narrow compositional range (Fo_{76-79}) and plagioclase are characterised by high An contents (An_{89-98}). Clinopyroxene varies from Mg# 70-80. Clinopyroxene crystals show minor Mg# zonation with a patchy distribution of higher Mg# zones throughout the sample (Supplementary Figure S4). The Ol-Cpx gabbro also contains a narrow range of olivine compositions (Fo_{77-80}) and plagioclase with high An (An_{90-}

$_{100}$). Clinopyroxene varies from Mg# 72-81 and individual crystals show minor Mg# zonation (Supplementary Figure S4).

Olivine in the banded gabbro varies from Fo$_{72-76}$. Plagioclase displays lower An (An$_{85-91}$) within the plag-cpx band (Figure 4b) compared with the matrix (~ An$_{90-97}$). Clinopyroxene within the plag-cpx band also have lower Mg# (69-74, Figure 4a,c), compared with the matrix (~ Mg# 73-80). Interstitial amphibole in the matrix have Mg# 62-70 (Supplementary Figure S3).

Olivine in the poikilitic gabbro varies from Fo$_{70-76}$. The An map for the poikilitic gabbro (Figure 5b) reveals the distribution of An variation in plagioclase in the sample and allows three populations to be identified, which are referred to as “high An”, “intermediate An” and “low An” in the remainder of the text. Rare high An (An$_{85-90}$) plagioclase (yellow on Figure 5b), typically found as crystal cores, are sparsely distributed throughout. The intermediate An (An$_{75-85}$) plagioclase population (orange on Figure 5b) are found as mantles to high An cores, as well as discrete crystals or crystal cores. The low An plagioclase (An$_{60-75}$) population (blue on Figure 5b) form rims on intermediate An population cores or discrete crystals. The clinopyroxene Mg# map for the poikilitic gabbro (Figure 5a) highlights the presence of two compositionally distinct clinopyroxene populations, which correspond to the two size populations observed in the sample. The first population includes clinopyroxene with Mg# 80-90 (pink and yellow in Figure 5a), which generally consists of the larger (> 1 mm) clinopyroxene crystals. Some of these crystals show minor reverse zoning with cores of Mg# ~82-85 and rims Mg# ~87-89. The second population (purple/blue in Figure 5a), corresponding to the smaller (generally < 1 mm) clinopyroxene crystals disseminated throughout the sample, have lower Mg# (70-80) with majority in the range Mg# 75-80. Some of these clinopyroxene display slight normal zoning with Mg# ~80 cores and Mg# ~76-78 overgrowths. These populations will be referred to as the “high Mg# Cpx” population (Mg# >

80) and "low Mg# Cpx" population (Mg# < 80) in the remainder of the text. Poikilitic gabbro amphibole have Mg# 65-70 and orthopyroxene Mg# 72-75 (Supplementary Figure S3).

Trace element chemistry of clinopyroxene and amphibole

Full trace element data for clinopyroxene and amphibole can be found in Supplementary Table ST2.

Clinopyroxene

Here we focus on the abundances of REE's, Zr and Y in clinopyroxene, which can discriminate between fractional crystallisation and melt-mush reaction in plutonic rocks (Lissenberg & MacLeod, 2016, Sanfillipo *et al*., 2020). Zirconium, Y and Ce broadly increase with decreasing Mg# (Figure 6a, b, c). Clinopyroxene from the olivine gabbro and Ol-Cpx gabbro have a similar range in Mg# and overlapping Zr, Y and Ce. Clinopyroxene in the banded gabbro matrix covers the same range but clinopyroxene within the plag-cpx band have elevated Ce and Zr relative to matrix, at lower Mg# (Figure 6). Clinopyroxene in the poikilitic gabbro spans the largest range of incompatible trace element concentrations. The lowest Zr, Y and Ce contents are found in the high Mg# Cpx, whereas the low Mg# Cpx from the same sample have higher Zr and Ce contents at a given Mg# compared with other samples.

Clinopyroxene from the olivine gabbro, Ol-Cpx gabbro and banded gabbro matrix have broadly similar curved REE patterns, with low LREE, relatively flat M-HREE (La = 0.15-0.4 µg/g, Yb = 1.04-1.96 µg/g, La_N/Yb_N = < 0.25, normalised to primitive mantle (Palme and O'Neill, 2003)), and small negative Eu anomalies (Figures 6 and 7). The plag-cpx band clinopyroxene have the same REE pattern as those from the banded gabbro matrix but are typically more REE enriched (La = 0.34-0.5 µg/g, Yb = 1.57-2.04 µg/g, La_N/Yb_N = < 0.25)

(Figure 6f, 7b). Most poikilitic gabbro high Mg# Cpx have similar REE patterns, but lower M-HREE contents, compared to clinopyroxene from other samples (La = 0.14-0.63 µg/g, Yb = 0.36-0.81 µg/g, La_N/Yb_N = 0.12-0.6). Poikilitic gabbro low Mg# Cpx have LREE enriched, almost flat REE profiles with similar M-HREE contents to clinopyroxene from other samples (La = 0.65-1.66 µg/g, Yb = 1.13-1.89 µg/g, La_N/Yb_N = 0.38-0.83) (Figure 6f, 7a). The concentrations of compatible elements such as Cr and Ni generally decrease with decreasing Mg# (Figure 6d, e). Poikilitic gabbro low Mg# Cpx show anomalously high Ni and Cr contents at a given Mg#.

Amphibole

Banded gabbro amphibole display a limited range in incompatible (Zr, Y, Ba, Nb) trace element concentrations (e.g. Nb = 0.6-1.1 µg/g, Figure 8a,b). In contrast, poikilitic gabbro amphibole are more enriched in incompatible trace elements and display a greater range (e.g. Nb = 8.5-12 µg/g, Figure 8a,b). Banded gabbro amphiboles are depleted in LREE relative to MREE/HREE (La = 0.59-0.87 µg/g, Yb = 2.08-3.38 µg/g, La_N/Yb_N = 0.16-0.23) and most have a small negative Eu anomaly (Figure 8d). Poikilitic gabbro amphibole are LREE enriched with almost flat REE patterns (La = 4.58-6.77 µg/g, Yb = 4.40-8.53 µg/g, La_N/Yb_N = 0.4-0.97) (Figure 8d). Five of the amphibole analyses from this sample are more enriched in Sm-Yb and have Eu anomalies. Banded gabbro amphibole have low abundances of the compatible elements Cr and Ni (Figure 8c), whereas poikilitic gabbro amphibole are enriched in these elements. We compare our data to compositions of amphibole from a range of plutonic xenoliths from Martinique, Lesser Antilles (Cooper *et al*., 2016) which display similar phase proportions and textural characteristics to those in St. Vincent.

DISCUSSION

In the following discussion, we attempt to infer the crystallisation conditions (pressure/depth-temperature) of our plutonic xenoliths and the possible compositions of the melts from which they crystallised, through comparison with the products of crystallisation experiments, following similar approaches applied successfully for other LAA plumbing systems (e.g. Cooper et al., 2016; Camejo-Harry et al. 2018; Melekhova et al., 2019; Fedele et al., 2021). We consider experiments which used lavas from both the LAA and other similar arc settings as starting materials.

We then use the estimated crystallisation conditions and our textural observations to guide our geochemical modelling of fractional crystallisation (FC) and melt-mush reaction. Our models focus on the REE compositions of clinopyroxene and amphibole, because mineral REE compositions have been shown to effectively distinguish between FC and melt-mush reaction processes in previous studies (e.g. Lissenberg & MacLeod, 2016; SanFillipo *et al.*, 2020; Boulanger *et al.*, 2021). Below, we will start with the simplest sample textures and build up complexity only as required by modelling results.

Evidence for fractional crystallisation

Olivine gabbro, Ol-Cpx gabbro, banded gabbro matrix

Comparison with experiments (Pichavant et al. 2018; Marxer et al., 2022) suggests that the plagioclase (An_{89-99}) – olivine (Fo_{72-80}) – clinopyroxene (Mg# 70-81) primocryst assemblage of the olivine gabbro, Ol-Cpx gabbro and banded gabbro matrix is consistent with crystallisation from a high-Al basalt melt with > 3.5 wt % H_2O at 975-1050°C, 0.2-0.6 GPa (~6-18 km depth, Supplementary Table ST4), in the mid-upper crust (assuming a ~29 km thick crust, Melekhova et al. 2019). Due to the absence of disequilibrium textures, such as embayed crystal cores or reaction relationships (e.g. amphibole replacing clinopyroxene rims) in the olivine gabbro and Ol-Cpx gabbro, we explored whether clinopyroxene REE compositions in these samples are consistent with fractional crystallisation from a basaltic parental melt (Models FC1 and FC2).

We modelled fractional crystallisation using the Rayleigh fractionation equation:

$$C_L = F^{(D-1)} * C_0 \qquad \text{[Eqn 1]}$$

where C_L = concentration of trace element in melt, C_0 = concentration of trace element in initial melt, F = fraction of melt remaining, D = bulk partition coefficient.

We present two FC models to illustrate the effect of varying the input parameters, which are poorly constrained in mushy magmatic systems. We used mineral-melt partition coefficients calculated using the model of Brophy (2008), which allowed us to predict partition coefficients for the mineral phases in the plutonic xenoliths as a function of coexisting melt SiO_2 content (Supplementary Table ST5). In experiments which reproduced the mineral assemblage and compositions of these samples (e.g. FM93, Marxer et al. 2022, Supplementary Table ST4), the co-existing melt is of basaltic composition. Hence, for models FC1 and FC2, we used partition coefficients at 49 wt % SiO_2, appropriate for a basaltic melt. In model FC1, the crystallising assemblage is based on the mineral phase abundances in the Ol-Cpx gabbro (plagioclase:olivine:clinopyroxene:magnetite in proportions 55:23:20:2), while model FC2 is based on the olivine gabbro (plagioclase:olivine:clinopyroxene:magnetite in proportions 69:22:8:1). The initial melt composition (HAB melt 1, Supplementary Table ST6) for model FC1 was calculated from the composition of a low-Yb clinopyroxene from the Ol-Cpx gabbro using clinopyroxene-melt partition coefficients at 49 wt % SiO_2. For model FC2, we used an initial melt composition (HAB melt 2, Supplementary Table ST6) with 20 % higher La and Ce than HAB melt 1. We consider our calculated melt compositions realistic, as they are similar to reported REE concentrations for basaltic melt inclusions from St Vincent (Bouvier et al. 2022**)**.

The results of models FC1 and FC2 show that the range of clinopyroxene REE compositions in the Ol-Cpx gabbro, olivine gabbro and banded gabbro matrix are generally reproduced by up to 60 % crystallisation of olivine + plagioclase + clinopyroxene + magnetite (Figure 9). Clinopyroxene compositions from the Ol-Cpx gabbro are best reproduced by model FC1, while olivine gabbro and banded gabbro matrix clinopyroxene compositions are better reproduced by model FC2 using an initial melt with a slightly higher LREE content. The model results suggest that clinopyroxene in these samples formed via closed system fractional crystallisation from a basaltic parental melt.

In the banded gabbro matrix, amphibole is texturally associated with and overgrowing the rims of clinopyroxene (Figure 2). This textural relationship indicates that amphibole formed via the peritectic reaction clinopyroxene + melt = amphibole, which may occur via two mechanisms; 1) reaction between trapped residual melt and clinopyroxene primocrysts during closed system crystallisation (e.g. Foden and Green, 1992; Chang *et al*., 2021) or 2) open system interactions between clinopyroxene primocrysts and percolating/migrating reactive melts (e.g. Foden & Green, 1992; Smith, 2014; Cooper *et al*., 2016).

To test mechanism 1, we assessed whether amphibole with REE compositions matching the banded gabbro amphibole could crystallise from the residual melt after 60-70 % crystallisation of the banded gabbro matrix primocryst assemblage (olivine + plagioclase + clinopyroxene + magnetite), simulated by model FC2. In experiments which reproduced the banded gabbro matrix primocryst assemblage + amphibole (e.g. HAB7, Pichavant et al. 2002, Supplementary Table ST4), the co-existing melt is of basaltic andesite composition. Therefore, we calculated amphibole compositions using partition coefficients at 53 wt % SiO_2

(Supplementary Table ST5). Figure 10e shows that amphibole crystallising from residual melts after 60-70 % crystallisation of the matrix primocryst assemblage closely match the banded gabbro amphibole REE compositions. Hence, we infer that the banded gabbro amphibole formed via a peritectic reaction between clinopyroxene and trapped interstitial melt during closed system crystallisation of the matrix. The banded gabbro amphibole REE patterns are distinct from the "interstitial" amphibole in plutonic xenoliths from Martinique (central LAA) (Figure 8d), which were formed via melt-mush reaction (Cooper et al., 2016). In Martinique, reactions with percolating melts formed amphiboles with greater enrichment in LREEs, and the resulting REE profiles are relatively flat (Figure 8d). Therefore, these distinctions rule out mechanism 2 and support our interpretation of a peritectic reaction between clinopyroxene and trapped interstitial melt during closed system crystallisation.

Poikilitic gabbro

Clinopyroxene with Mg# > 80, matching the high Mg# Cpx population in the poikilitic gabbro (Figure 5a), have been produced in crystallisation experiments using St Vincent high-Mg basalt starting compositions at 1050-1200 °C, and both lower (1 GPa/~30 km depth) and mid-crustal (0.4 GPa/~12 km depth) pressures (Pichavant and Macdonald, 2007; Melekhova *et al.* 2015, Supplementary Table ST4). The high An_{85-90} plagioclase population (Figure 5b) and olivine (Fo_{70-76}) are consistent with crystallisation from a high-Al basalt melt at 975-1050°C, ~6-18 km depth (Pichavant *et al.* 2018; Marxer *et al.*, 2022; Supplementary Table ST4). The intermediate and lower An (An_{60-85}) plagioclase populations, low Mg# clinopyroxene, amphibole and orthopyroxene compositions are consistent with crystallisation from high-Al basalt to andesitic melts at 875-1000 °C, 5-12 km depth (Martel *et al.* 1999; Blatter *et al.* 2013; Pichavant *et al.* 2018; Marxer *et al.*, 2023, Supplementary Table ST4).

In experiments, high Mg# clinopyroxene co-crystallises with high Fo (typically > 80) olivine and spinel (Pichavant and Macdonald, 2007; Melekhova *et al*., 2015) producing residual high-Al basalt melts. Since the poikilitic gabbro does not contain high Fo olivine or spinel, we infer that the high Mg# clinopyroxene represent a crystal cargo carried in a parental high-Al basalt melt, which crystallised the high An plagioclase and low Fo olivine. Alternatively, if high Fo olivine were also among the crystal cargo, these crystals could have re-equilibrated to lower Fo compositions. We suggest that the high Mg# clinopyroxene crystallised from primitive high-Mg basalt melts and that the trace element compositional variation within this crystal population could reflect variations in primitive magma compositions beneath St Vincent, which likely result from partial melting of a mantle source variably metasomatized by different slab derived fluids/sediment melts (Bouvier et al., 2010).

The high An plagioclase are only found as crystal cores and olivine is rimmed by poikilitic orthopyroxene and amphibole. These textural relationships and the inferred crystallisation temperatures based on experimental comparisons (above) suggest that the high An plagioclase and olivine crystallised prior to the intermediate and low An plagioclase + low Mg# clinopyroxene + orthopyroxene + amphibole. We infer that the low Mg# clinopyroxene co-crystallise with the intermediate An plagioclase population, rather than with the high An plagioclase and olivine, due to the presence of small low Mg# Cpx inclusions in intermediate An plagioclase (Figure 3e). We modelled this latter crystallisation stage (model FC3) to assess whether the REE compositions of the poikilitic gabbro low Mg# clinopyroxene and amphibole are consistent with fractional crystallisation.

For model FC3, we used a crystallising assemblage of plagioclase + clinopyroxene + amphibole + orthopyroxene in proportions 50:10:20:20, estimated from the modal abundances of these crystal populations in the sample. In experiments which reproduced this assemblage (e.g. run 2390, Blatter et al. 2013, Supplementary Table ST4) the co-existing melt is of andesitic composition. Assuming a $KD^{(Fe\text{-}Mg)}$cpx/melt of 0.28 ± 0.08 (Putirka, 2008) and $KD^{(Fe\text{-}Mg)}$opx/melt of 0.28 ± 0.04 (Beattie, 1993), melts in equilibrium with the low Mg# Cpx and orthopyroxene have estimated Mg# 40-58 and Mg# 38-49 respectively, within the range of andesite (Mg# 48-24) glasses from St Vincent scoria (Fedele et al., 2021). Amphibole in previously studied St Vincent plutonic xenoliths (Tollan et al. 2012) are in equilibrium with andesitic melts (58-63 % SiO_2, calculated using the model of Humphreys et al. 2019). Therefore, we used partition coefficients for a coexisting melt with 59 wt % SiO_2 (Brophy 2008; Nandedkar et al., 2016 for amphibole, Supplementary Table ST5). We used the composition of a basaltic melt inclusion from St Vincent (svn4b-184, Bouvier et al. 2022; Supplementary Table ST6) as the initial melt composition, to represent the residual melt after initial crystallisation of the high An plagioclase and low Fo olivine.

The range of REE compositions displayed by the poikilitic gabbro low Mg# clinopyroxene and amphibole are not well reproduced by model FC3 (Figures 11 and 12). In addition, poikilitic gabbro amphibole Ni concentrations show a positive correlation with La and Zr (Supplementary Figure S5). Based on typical partition coefficients from the GERM database (https://earthref.org/GERM), Ni is expected to be compatible in the crystallising assemblage while La and Zr are incompatible, which would result in a negative correlation between these elements in amphibole formed during fractional crystallisation. Despite the uncertainties regarding selection of the model input parameters, our modelling results using plausible inputs and the mineral compositions strongly suggest that the low Mg# clinopyroxene and amphibole are not products of fractional crystallisation.

Evidence for Melt-mush reaction

Poikilitic gabbro

The mineral textures in the poikilitic gabbro suggest that open system melt-mush reaction processes contributed to the petrogenesis of this sample. The high An plagioclase population takes the form of relict or patchy cores. These plagioclase textures, and the embayed appearance of the olivine and clinopyroxene rimmed by orthopyroxene and amphibole, closely resemble textures created by dissolution in experiments simulating melt-mush and melt-rock reaction (Yang *et al*., 2019; Wang *et al*., 2021). In similar experiments simulating contamination of a magma with foreign crystals and micro-xenoliths (Erdmann *et al*., 2010), many of the contaminant crystals (analogous to initial mush crystals in a melt-mush reaction scenario) acquired rounded/embayed textures akin to the poikilitic gabbro olivine and high Mg# clinopyroxene. Hence, we suggest that the high An plagioclase, olivine and high-Mg# clinopyroxene are derived from an initial mush modified by melt-mush reaction. The low Mg# clinopyroxene compositions are inconsistent with fractional crystallisation (Figure 11). Therefore, we suggest that these crystals formed as a reaction product, along with the intermediate An plagioclase surrounding relict high An cores, and poikilitic amphibole and orthopyroxene.

We propose that the poikilitic gabbro records the following melt-mush reaction: olivine + high An plagioclase + high Mg# clinopyroxene + melt -> low Mg# clinopyroxene + intermediate An plagioclase + orthopyroxene + amphibole + melt 2. To test this hypothesis, we modelled this reaction (model AFC1) using the Assimilation-Fractional Crystallisation (AFC) equations of DePaolo (1981), following the approach of previous studies of melt-mush reaction in mid-ocean ridge gabbros (e.g. SanFillipo *et al*., 2020; Boulanger *et al*., 2020, 2021; Ferrando *et al*., 2021).

AFC equation from DePaolo (1981):

$$C_L = \left(F^{-Z} + \left(\frac{r}{r-1} \times \frac{C_a}{(Z \times C_0)} \times 1 - F^{-Z}\right)\right) \times C_0 \qquad \text{[Eqn 3]}$$

where C_L = concentration of trace element in melt, C_0 = concentration of trace element in initial melt, C_a = concentration of trace element in assimilant, F = fraction of melt remaining, Z = (r+D-1)/(r-1), D = bulk partition coefficient, r = rate of assimilation/rate of crystal fractionation**.**

The equation explicitly accounts for trace element contributions from both the initial reactive melt and crystals in the pre-existing mush (the assimilant); therefore, we consider it appropriate for modelling our proposed melt-mush reaction scenario.

It is difficult to determine the proportions of phases formed in our proposed reaction from textural inspection alone. For model AFC1, we infer a crystallising assemblage of plagioclase + clinopyroxene + amphibole + orthopyroxene in proportions 50:10:20:20, which approximates the relative proportions of the reaction product crystal populations in the poikilitic gabbro. Model AFC1 was tested with up to 5 % variations in the mineral proportions listed above, which does not significantly change the results. Adjusting the mineral proportions has a less significant influence on model results than adjusting other parameters such as the "r" value, which we vary over a wide range of plausible values in our model (see below). Our proposed reaction product assemblage is likely in equilibrium with andesitic melts (see previous section), therefore, we used partition coefficients for a coexisting melt with 59 wt % SiO_2 (Supplementary Table ST5).

The presence of orthopyroxene replacing olivine rims suggests that the invading reactive melt had a relatively high SiO_2 content, and the compositions of the inferred reaction product phases are similar to products of crystallisation experiments using andesite starting materials (Martel *et al*., 1999; Pichavant *et al*., 2018, Supplementary Table ST4). Available trace element data for St Vincent melt inclusions only covers basaltic and dacitic compositions (Bouvier *et al*. 2022; Balcone-Boissard *et al*. 2023). To represent an andesitic initial reactive melt composition, we used the REE composition of an andesitic melt inclusion from the northern LAA island of St Kitts (Toothill et al. 2007) ("Kit 15", Supplementary Table ST6). The REE content and ratios (La/Yb =1.9, Ce/Yb = 4.8) of this melt inclusion are similar to published values for St Vincent melt inclusions (La/Yb =1.6-2.3, Ce/Yb = 4.1-7.1, Bouvier *et al.* 2022; Balcone-Boissard *et al.* 2023) therefore we consider it a plausible input for our models.

Published trace element data for St Vincent plutonic xenolith whole-rock or mineral compositions is very limited (only Dostal *et al*., 1983). Therefore, for the assimilant composition, we used the whole-rock REE composition of a plutonic xenolith from Martinique (sample MQ44, Cooper *et al*., 2016, Supplementary Table ST6). This sample contains plagioclase (An > 90, 78 %), olivine (Fo_{76-79}, 16 %) and high Mg# (82-89) clinopyroxene (6 %), and thus approximates our inferred initial mush assemblage.

Model AFC1 reproduces the variation in REE compositions of the low Mg# clinopyroxene and most of the amphibole, using r = 0.55-0.8, after 30-70 % crystallisation (clinopyroxene, Figure 11) and r = 0.15-0.4, after 80-90 % crystallisation (amphibole, Figure 12). The discrepancy in extent of crystallisation required to reproduce the clinopyroxene and amphibole compositions may reflect variations in the proportions of mineral phases crystallising as the reaction proceeds. The range of r values required to produce the mineral REE compositions may reflect localised variations in the extent of disequilibrium between initial mush crystals and infiltrating reactive melt (e.g. Ferrando et al. 2021), resulting in regions of preferential assimilation (higher r values).

The combination of AFC models using realistic input parameters, and our detailed textural analysis of mineral phases strongly imply a role for melt-mush reaction in the petrogenesis of the poikilitic gabbro. We infer that an initial mush composed of olivine + high An plagioclase + high Mg# clinopyroxene was infiltrated by an evolved, likely andesitic reactive melt (Figure 13, a). Melt-mush reaction triggered partial dissolution of the initial mush minerals, and crystallisation of the intermediate An plagioclase + low Mg# clinopyroxene + orthopyroxene + amphibole (Figure 13, b). Following melt-mush reaction, we propose that amphibole continued to crystallise from the residual melt, along with the An_{60-75} plagioclase (explaining the lower An plagioclase inclusions in poikilitic amphibole) and interstitial apatite (Figure 13, c). This interpretation is consistent with experiments simulating typical arc magma crystallisation sequences which produce amphibole + plagioclase + apatite assemblages in the lower temperature stages (Nandedkar *et al*., 2014; Marxer *et al*., 2022).

Plag-Cpx band

The "plag-cpx band" in the banded gabbro is one centimetre wide and distinguished from the surrounding matrix by the absence of olivine, lower Mg# clinopyroxene and lower An plagioclase with inclusion rich cores (Figure 4, Supplementary Figure S2). The contact between the matrix and plag-cpx band, as defined by the chemical map, cross-cuts some clinopyroxene crystals (Figure 4c). In these clinopyroxene crystals, the matrix portion of the crystals have higher Mg# than the portion in the band (Figure 4c). The lower Mg# compositions (Mg# 69-74) only occur within portions of clinopyroxene within the discrete band. The lower Mg# compositions are not represented elsewhere in the sample matrix. This suggests that the band formed via melt-mush reaction when a spatially constrained migrating melt interacted with the matrix primocryst clinopyroxene. We rule out the possibility that the band represents an intrusion through a solidified cumulate (i.e. a body of mush which has fully crystallised) because there is no evidence for brittle deformation or a chilled margin.

The absence of olivine in the plag-cpx band and olivine-gabbro assemblage of the matrix is consistent with the reaction: olivine + plagioclase + clinopyroxene + melt -> plagioclase 2 + clinopyroxene 2 + melt 2, which is a common melt-mush reaction in mid-ocean ridge magmatic plumbing systems (SanFillipo *et al*., 2020; Boulanger *et al*., 2021; Ferrando *et al*., 2021; Boulanger & France, 2023). We tested whether this melt-mush reaction can reproduce the REE compositions of the plag-cpx band clinopyroxene using model AFC2. For this model, we used a crystallising assemblage of plagioclase + clinopyroxene + magnetite in proportions 50:49:1, which approximates the relative mineral phase proportions of the plag-cpx band. We used partition coefficients for a coexisting melt with 49 wt % SiO_2 (Supplementary Table ST5), the HAB melt 2 initial melt composition (Supplementary Table ST6), and the same assimilant composition as model AFC1 (MQ44, Supplementary Table ST6), which approximates an initial olivine gabbro mush.

Model AFC2 closely reproduces the REE compositions of the plag-cpx band clinopyroxene, using r = 0.4, after 50-60 % crystallisation (Figure 10). Therefore, the model results support a melt-mush reaction origin for the plag-cpx band. It should be noted that using our chosen input parameters, fractional crystallisation of the plag-cpx band assemblage (r = 0 on Figure 10) can also quite closely reproduce the REE compositions of the clinopyroxene within the band. Hence, the clinopyroxene REE compositions and modelling in isolation do not provide unequivocal evidence for melt-mush reaction in this sample, without the textural context provided by the sample element map.

We propose that the plag-cpx band formed through a “reactive infiltration feedback” mechanism (Ortoleva *et al*., 1987) (Figure 14). In this model, the flux of reactive supercritical hydrous melt through a porous crystal mush framework is greater in regions of initially higher porosity, causing the mush crystals to dissolve faster in these regions. This process results in positive feedback and focuses the flux of reactive supercritical hydrous melt into a narrower region as more rock is dissolved. This concept may explain how reactive melts percolating through an initial olivine gabbro mush became focused into a centimetre wide region to form the plag-cpx band (Figure 14). Recent thermodynamic simulations of melt-mush reaction have demonstrated a similar melt channelisation process (Gleeson *et al*., 2023) and the same process was used to explain a mechanism by which dunite channels form in mantle peridotites (Kelemen *et al*., 1995). The thickness of such channels is variable but in examples from the Oman ophiolite, can be as low as one centimetre (Braun & Kelemen, 2002). Similar distinct centimetre sized bands interpreted to have formed via melt-mush reaction are found in MOR plutonic rocks (Lissenberg & MacLeod, 2016; SanFillipo *et al*., 2020; Ferrando *et al*., 2021) and layered intrusions (Namur *et al.*, 2013; Hepworth *et al*., 2020) suggesting that this is a common process in mushy plutonic environments.

Influence of melt-mush reaction on St Vincent magma compositions

In Figure 15, we compare the estimated REE compositions of melts in equilibrium with plutonic xenolith mineral phases interpreted as melt-mush reaction products (plag-cpx band clinopyroxene, poikilitic gabbro low Mg# Cpx and amphibole) with St Vincent lavas (whole-rock) and melt inclusions. The equilibrium melts overlap both lava and melt inclusion compositions, suggesting that melt-mush reaction could cryptically influence magma trace element compositions in the St Vincent plumbing system. The overlap between equilibrium melts and lavas, which have trace element compositions consistent with FC (Heath et al. 1998, Fedele et al., 2021) corroborates our geochemical modelling results for the banded gabbro, demonstrating that melt-mush reaction may not always produce melt or mineral trace element compositions that can be clearly distinguished from FC in arc plumbing systems. Similarly, buffering of melt major element compositions during the reaction process (e.g. Blundy, 2022) may obscure records of melt-mush reaction when investigating the composition of glass and whole-rock samples.

The plutonic xenolith record of the St Vincent plumbing system

Comparison with experiments suggests that our plutonic xenoliths are derived from mush stored in the mid-upper crust within the plumbing system beneath St Vincent. Their textures and mineral compositions demonstrate that in addition to fractional crystallisation, melt-mush reaction processes operate and influence magma chemical evolution. Of the seventeen plutonic xenoliths initially assessed via optical petrology for this study (Supplementary Table ST1), only the two hornblende-olivine gabbros (banded and poikilitic gabbro) contain clear textural evidence for melt-mush reaction. Textures indicative of melt-mush reaction were not reported from St Vincent plutonic xenoliths (n=17) studied by Tollan *et al.*, (2012), which have mineral Oxygen isotopic compositions consistent with FC and similar mineral compositions to our olivine gabbros (plagioclase An_{85-95}, olivine Fo_{71-79}, clinopyroxene Mg# 75-81). Several of these samples contain amphiboles displaying well equilibrated contacts with other mineral phases (Tollan et al., 2012), in contrast to the amphibole replacing embayed clinopyroxene/olivine margins in our poikilitic gabbro sample. Lewis (1973) described < 1cm thick bands and layers in St Vincent plutonic xenoliths which broadly resemble the banded gabbro, and poikilitic amphibole/orthopyroxene replacing the rims of clinopyroxene/olivine have been reported (but not studied in detail) in individual St Vincent plutonic xenoliths (Hu et al., 2022; Weber et al., 2024).

The low frequency of evidence for melt-mush reaction among the wider St Vincent plutonic xenolith suite studied to date may indicate that FC represents the dominant magma chemical evolution process in the plumbing system. However, exposed crustal sections of extinct arcs and layered intrusions show that melt-mush reaction often modifies highly localised regions of mush, which take the form of centimetre-decimetre thick bands with distinct mineral assemblages, dispersed across 1-100’s of metres of outcrop (Namur *et al*., 2013; Boulanger *et al*., 2021; Nixon et al., 2024). Therefore, it is plausible that portions of mush that have been modified by melt-mush reaction may be less likely to be sampled as plutonic xenoliths compared to unmodified portions of mush.

Implications for magma chemical evolution in arc systems

Several studies of plutonic xenoliths from the LAA and other active arc settings have established that fractional crystallisation is a key process controlling the chemical evolution of arc magmas (Arculus and Wills, 1980; Conrad and Kay, 1984; Tollan et al., 2012; Haase et al., 2014; Whitley et al, 2024). Plutonic xenoliths bearing textural and/or chemical evidence for melt-mush reaction have also been documented throughout the LAA (Stamper *et al*., 2014; Cooper *et al*., 2016; Melekhova *et al*., 2017; Camejo-Harry *et al*., 2018, 2024), other active arc systems (Costa *et al*., 2002; Smith, 2014; Klaver *et al*., 2017) and exhumed arc crustal sections (Bouilhol *et al*., 2015; Villares *et al*., 2022; Li *et al*., 2024; Nixon et al., 2024). Hence, we infer that melt-mush reaction, in addition to fractional crystallisation, is a common, and likely ubiquitous feature of mush dominated arc plumbing systems. Therefore, melt-mush reaction represents an important process contributing to the diversity of arc magma trace element compositions and for generating local heterogeneity in the trace element composition of arc crust formed at subduction zones.

Our study shows that melt-mush reaction is a cryptic process in active arc systems and can only be identified through a detailed textural and chemical study of plutonic xenoliths. Our results also highlight that it can be difficult to distinguish mineral and melt compositions produced during melt-mush reaction from those produced during FC in arc systems. Our ability to identify and understand melt-mush reaction processes in arc plumbing systems could be advanced through future detailed studies of plutonic xenoliths, as well as experimental studies which simulate melt-mush reaction and quantify mineral-melt trace element partitioning under arc crustal conditions (e.g. Nandedkar et al., 2016), and/or development of more advanced geochemical/thermodynamic models for simulating the complexities of melt-mush reaction.

CONCLUSIONS

In this study, we investigated a suite of plutonic xenoliths from St Vincent, Lesser Antilles arc, where lava compositions follow fractional crystallisation trends, to directly assess the processes controlling magma chemical evolution in the mush dominated plumbing system of an active arc volcano. We suggest that the absence of disequilibrium textures, mineral major element and clinopyroxene trace element chemistry of olivine gabbro xenoliths are consistent with fractional crystallisation in the mid-upper crust. In contrast, both the "banded gabbro" and "poikilitic gabbro" samples (hornblende-olivine gabbros) from the mid-upper crust contain textural and chemical evidence for melt-mush reaction. Clinopyroxene and amphibole trace element compositions in the "poikilitic gabbro" are best reproduced by assimilation-fractional crystallisation models, simulating melt-mush reaction. The "banded gabbro" contains a centimetre wide band with distinct mineralogy and mineral chemistry to the surrounding olivine gabbro matrix, which we interpret to have formed via melt-mush reaction as reactive melts percolating through an initial olivine gabbro mush were focused into a channel.

Plutonic xenoliths displaying textural evidence for melt-mush reaction are relatively uncommon among the wider suite of St Vincent plutonic xenoliths analysed in our study and by previous authors. St. Vincent lavas and plutonic xenoliths therefore suggest that fractional crystallisation is likely the dominant process controlling magma evolution within the plumbing system beneath St Vincent. However, our plutonic xenoliths demonstrate that melt-mush reaction is also a significant process operating in the St. Vincent plumbing system which cryptically influences the trace element compositions of St Vincent magmas.

Our study highlights both the importance of studying the plutonic record alongside the eruptive record and combining geochemical modelling with a detailed evaluation of the textural relationships between mineral phases and the spatial records of mineral chemistry to investigate the processes controlling the chemical diversity of active arc plumbing systems. Textures indicative of melt-mush reaction have been observed in plutonic xenoliths throughout the Lesser Antilles and in other active arcs and exhumed arc crustal sections. We therefore suggest that melt-mush reaction is likely a ubiquitous process in arc plumbing systems, which exerts a cryptic control on the trace element compositions of subduction zone magmas and arc crust.

Funding

This work was supported by a NERC IAPETUS DTP PhD studentship awarded to JB and the VoiLA NERC consortium grant (NE/K010824/1). GFC is currently funded by a Royal Society University Research Fellowship 2022 and acknowledges previous funding by the VoiLA NERC consortium grant (NE/K010824/1).

Acknowledgements

JB acknowledges the support of a NERC IAPETUS DTP PhD studentship. We would like to thank Kevin Burton and Dan Morgan for comments on an earlier version of this manuscript. We appreciate the support of Kemron Alexander and Richard Robertson during fieldwork and sample collection in St Vincent, and Duncan Muir for facilitating thin section chemical mapping at Cardiff University. We thank two anonymous reviewers and Manuel Pimenta

Silva for their thorough and constructive reviews which greatly improved the manuscript, and Tod Waight for editorial handling.

Data availability

The data underlying this article are available in the article and in its online supplementary material. The data underlying this article are available in [EarthChem Library] – at https://doi.org/10.60520/IEDA/113444.

References

Arculus, R. J. & Wills, K. J. A. (1980). The Petrology of Plutonic Blocks and Inclusions from the Lesser Antilles Island Arc. *Journal of Petrology* **21**, 743–799.

Bachmann, O. & Bergantz, G.W. (2004). On the origin of crystal-poor rhyolites: extracted from batholithic crystal mushes. *Journal of Petrology 45*(8), 1565-1582.

Bachmann, O. & Huber, C. (2019). The inner workings of crustal distillation columns; the physical mechanisms and rates controlling phase separation in silicic magma reservoirs. *Journal of Petrology 60*(1), 3-18.

Beattie, P. (1993). Olivine-melt and orthopyroxene-melt equilibria. *Contributions to Mineralogy and Petrology* **115**, 103–111.

Blatter, D. L., Sisson, T. W. & Hankins, W. B. (2013). Crystallization of oxidized, moderately hydrous arc basalt at mid- to lower-crustal pressures: implications for andesite genesis. *Contributions to Mineralogy and Petrology* **166**, 861–886.

Blundy, J. (2022). Chemical Differentiation by Mineralogical Buffering in Crustal Hot Zones. *Journal of Petrology* **63**, egac054.

Bouilhol, P., Schmidt, M. W. & Burg, J.-P. (2015). Magma Transfer and Evolution in Channels within the Arc Crust: the Pyroxenitic Feeder Pipes of Sapat (Kohistan, Pakistan). *Journal of Petrology* **56**, 1309–1342.

Boulanger, M., France, L., Deans, J. R., Ferrando, C., Lissenberg, J. C. & von der Handt, A. (2020). Magma Reservoir Formation and Evolution at a Slow-Spreading Center (Atlantis Bank, Southwest Indian Ridge). *Frontiers in Earth Science* **8**, 554598.

Boulanger, M., France, L., Ferrando, C., Ildefonse, B., Ghosh, B., Sanfilippo, A., Liu, C.Z., Morishita, T., *et al.* (2021). Magma-Mush Interactions in the Lower Oceanic Crust: Insights From Atlantis Bank Layered Series (Southwest Indian Ridge). *Journal of Geophysical Research: Solid Earth* **126**, e2021JB022331.

Boulanger, M. & France, L. (2023). Cumulate Formation and Melt Extraction from Mush-Dominated Magma Reservoirs: The Melt Flush Process Exemplified at Mid-Ocean Ridges. *Journal of Petrology* **64**, egad005.

Bouvier, A.-S., Deloule, E. & Métrich, N. (2010). Fluid Inputs to Magma Sources of St. Vincent and Grenada (Lesser Antilles): New Insights from Trace Elements in Olivine-hosted Melt Inclusions. *Journal of Petrology* **51**, 1597–1615.

Bouvier, A.-S., Rose-Koga, E. F., Nichols, A. R. L. & Le Lay, C. (2022). Melt inclusion formation during olivine recrystallization: Evidence from stable isotopes. *Earth and Planetary Science Letters* **592**, 117638.

Braun, M. G. & Kelemen, P. B. (2002). Dunite distribution in the Oman Ophiolite: Implications for melt flux through porous dunite conduits. *Geochemistry, Geophysics, Geosystems* **3**, 1–21.

Brophy, J. G. (2008). A study of rare earth element (REE)–SiO2 variations in felsic liquids generated by basalt fractionation and amphibolite melting: a potential test for discriminating between the two different processes. *Contributions to Mineralogy and Petrology* **156**, 337–357.

Camejo-Harry, M., Melekhova, E., Blundy, J., Attridge, W., Robertson, R. & Christopher, T. (2018). Magma evolution beneath Bequia, Lesser Antilles, deduced from petrology of lavas and plutonic xenoliths. *Contributions to Mineralogy and Petrology* **173**, 77.

Camejo-Harry, M., Melekhova, E., Aufrère, S., McCarthy, A. & Blundy, J. (2024). Early arc crust formation preserved in the Grenadines archipelago, southern Lesser Antilles arc. *Royal Society Open Science* **11**, 231914.

Cashman, K. V., Sparks, R. S. J. & Blundy, J. D. (2017). Vertically extensive and unstable magmatic systems: A unified view of igneous processes. *Science* **355**, eaag3055.

Chadwick, J. P., Troll, V. R., Waight, T. E., van der Zwan, F. M. & Schwarzkopf, L. M. (2013). Petrology and geochemistry of igneous inclusions in recent Merapi deposits: a window into the sub-volcanic plumbing system. *Contributions to Mineralogy and Petrology* **165**, 259–282.

Chang, J., Audétat, A. & Li, J.-W. (2021). *In situ* Reaction-replacement Origin of Hornblendites in the Early Cretaceous Laiyuan Complex, North China Craton, and Implications for its Tectono-magmatic Evolution. *Journal of Petrology* **62**, egab030.

Cole, P. D., Robertson, R. E. A., Fedele, L. & Scarpati, C. (2019). Explosive activity of the last 1000 years at La Soufrière, St Vincent, Lesser Antilles. *Journal of Volcanology and Geothermal Research* **371**, 86–100.

Conrad, W.K. & Kay, R.W. (1984). Ultramafic and mafic inclusions from Adak Island: crystallization history, and implications for the nature of primary magmas and crustal evolution in the Aleutian Arc. *Journal of Petrology*, **25**(1), 88-125.

Cooper, G. F., Davidson, J. P. & Blundy, J. D. (2016). Plutonic xenoliths from Martinique, Lesser Antilles: evidence for open system processes and reactive melt flow in island arc crust. *Contributions to Mineralogy and Petrology* **171**, 87.

Cooper, G. F., Blundy, J. D., Macpherson, C. G., Humphreys, M. C. S. & Davidson, J. P. (2019). Evidence from plutonic xenoliths for magma differentiation, mixing and storage in a volatile-rich crystal mush beneath St. Eustatius, Lesser Antilles. *Contributions to Mineralogy and Petrology* **174**, 39.

Cooper, G. F., Macpherson, C. G., Blundy, J. D., Maunder, B., Allen, R. W., Goes, S. *et al.* (2020). Variable water input controls evolution of the Lesser Antilles volcanic arc. *Nature* **582**, 525–529.

Cooper, G. F., Lissenberg, C. J., Koorneef, J. M., Jansen, M. N., & Millet, M. A. (2025). Crustal versus mantle-level aggregation of heterogeneous melts at mid-ocean ridges. *Geology* **53**, 430-434.

Costa, F., Dungan, M. A. & Singer, B. S. (2002). Hornblende- and Phlogopite-Bearing Gabbroic Xenoliths from Volca´n San Pedro (36°S), Chilean Andes: Evidence for Melt and Fluid Migration and Reactions in Subduction-Related Plutons. *Journal of Petrology* **43**, 219-241.

Davidson, J. P., Hora, J. M., Garrison, J. M. & Dungan, M. A. (2005). Crustal forensics in arc magmas. *Journal of Volcanology and Geothermal Research* **140**, 157–170.

Davidson, J. P., Morgan, D. J., Charlier, B. L. A., Harlou, R. & Hora, J. M. (2007). Microsampling and Isotopic Analysis of Igneous Rocks: Implications for the Study of Magmatic Systems. *Annual Review of Earth and Planetary Sciences* **35**, 273–311.

DePaolo, D. J. (1981). Trace element and isotopic effects of combined wallrock assimilation and fractional crystallization. *Earth and Planetary Science Letters* **53**, 189–202.

Dostal, J., Dupuy, C., Carron, J. P., Le Guen de Kerneizon, M. & Maury, R. C. (1983). Partition coefficients of trace elements: Application to volcanic rocks of St. Vincent, West Indies. *Geochimica et Cosmochimica Acta* **47**, 525–533.

DuFrane, S. A., Turner, S., Dosseto, A. & van Soest, M. (2009). Reappraisal of fluid and sediment contributions to Lesser Antilles magmas. *Chemical Geology* **265**, 272–278.

Edmonds, M., Cashman, K. V., Holness, M. & Jackson, M. (2019). Architecture and dynamics of magma reservoirs. *Philosophical Transactions of the Royal Society A: Mathematical, Physical and Engineering Sciences*. Royal Society **377**, 20180298.

Erdmann, S., Scaillet, B. & Kellett, D. A. (2010). Xenocryst assimilation and formation of peritectic crystals during magma contamination: An experimental study. *Journal of Volcanology and Geothermal Research* **198**, 355–367.

Fedele, L., Cole, P. D., Scarpati, C. & Robertson, R. E. A. (2021). Petrological insights on the last 1000 years of explosive activity at La Soufrière volcano, St. Vincent (Lesser Antilles). *Lithos* **392–393**, 106150.

Ferrando, C., France, L., Basch, V., Sanfilippo, A., Tribuzio, R. & Boulanger, M. (2021). Grain Size Variations Record Segregation of Residual Melts in Slow-Spreading Oceanic Crust (Atlantis Bank, 57°E Southwest Indian Ridge). *Journal of Geophysical Research: Solid Earth* **126**, e2020JB020997.

Foden, J. D. & Green, D. H. (1992). Possible role of amphibole in the origin of andesite: some experimental and natural evidence. *Contributions to Mineralogy and Petrology* **109**, 479–493.

Gleeson, M. L. M., Gibson, S. A. & Stock, M. J. (2021). Upper Mantle Mush Zones beneath Low Melt Flux Ocean Island Volcanoes: Insights from Isla Floreana, Galápagos. *Journal of Petrology* **61**, egaa094.

Gleeson, M. L. M., Lissenberg, C. J. & Antoshechkina, P. M. (2023). Porosity evolution of mafic crystal mush during reactive flow. *Nature Communications* **14**, 3088.

GERM partition coefficient database. https://earthref.org/GERM. (accessed 28th August 2025).

Haase, K. M., Lima, S., Krumm, S. & Garbe-Schönberg, D. (2014). The magmatic evolution of young island arc crust observed in gabbroic to tonalitic xenoliths from Raoul Island, Kermadec Island Arc. *Lithos* **210–211**, 199–208.

Heath, E., Macdonald, R., Belkin, H., Hawkesworth, C. & Sigurdsson, H. (1998). Magmagenesis at Soufriere Volcano, St Vincent, Lesser Antilles Arc. *Journal of Petrology* **39**, 1721-1764.

Hélène, B.-B., Georges, B., Thiébaut, d'Augustin, Saskia, E., Etienne, D. & Juliette, V. (2023). Architecture of the Lesser Antilles Arc Illustrated by Melt Inclusions. *Journal of Petrology* **64**, egad020.

Hepworth, L. N., Daly, J. S., Gertisser, R., Johnson, C. G., Emeleus, C. H. & O'Driscoll, B. (2020). Rapid crystallization of precious-metal-mineralized layers in mafic magmatic systems. *Nature Geoscience* **13**, 375–381.

Hildreth, W. & Moorbath, S. (1988). Crustal contributions to arc magmatism in the Andes of Central Chile. *Contributions to Mineralogy and Petrology* **98**, 455–489.

Hu, H., Jackson, M. D. & Blundy, J. (2022). Melting, Compaction and Reactive Flow: Controls on Melt Fraction and Composition Change in Crustal Mush Reservoirs. *Journal of Petrology* **63**, egac097.

Humphreys, M. C. S., Cooper, G. F., Zhang, J., Loewen, M., Kent, A. J. R., Macpherson, C. G. & Davidson, J. P. (2019). Unravelling the complexity of magma plumbing at Mount St. Helens: a new trace element partitioning scheme for amphibole. *Contributions to Mineralogy and Petrology* **174**, 9.

Humphreys, M.C., Namur, O., Bohrson, W.A., Bouilhol, P., Cooper, G.F., Cooper, K.M., Huber, C., Lissenberg, C.J., Morgado, E. & Spera, F.J. (2025). Crystal mush processes and crustal magmatism. *Nature Reviews Earth & Environment* 6, 401–416.

Jackson, M. D., Blundy, J. & Sparks, R. S. J. (2018). Chemical differentiation, cold storage and remobilization of magma in the Earth's crust. *Nature* **564**, 405–409.

Jochum, K. P., Nohl, U., Herwig, K., Lammel, E., Stoll, B. & Hofmann, A. W. (2005). GeoReM: A New Geochemical Database for Reference Materials and Isotopic Standards. *Geostandards and Geoanalytical Research* **29**, 333–338.

Jochum, K. P., Weis, U., Stoll, B., Kuzmin, D., Yang, Q., Raczek, I., Jacob, D. E., Stracke, A., Birbaum, K., Frick, D. A., Günther, D. & Enzweiler, J. (2011). Determination of Reference Values for NIST SRM 610–617 Glasses Following ISO Guidelines. *Geostandards and Geoanalytical Research* **35**, 397–429.

Kelemen, P. B., Whitehead, J. A., Aharonov, E. & Jordahl, K. A. (1995). Experiments on flow focusing in soluble porous media, with applications to melt extraction from the mantle. *Journal of Geophysical Research: Solid Earth* **100**, 475–496.

Klaver, M., Matveev, S., Berndt, J., Lissenberg, C. J. & Vroon, P. Z. (2017). A mineral and cumulate perspective to magma differentiation at Nisyros volcano, Aegean arc. *Contributions to Mineralogy and Petrology* **172**, 95.

Lewis, J. F. (1973). Petrology of the Ejected Plutonic Blocks of the Soufrière Volcano, St. Vincent, West Indies. *Journal of Petrology* **14**, 81–112.

Li, J.-Y., Wang, X.-L., Gu, Z.-D., Wang, D. & Du, D.-H. (2024). Geochemical diversity of continental arc basaltic mushy reservoirs driven by reactive melt infiltration. *Communications Earth & Environment* **5**, 1–11.

Lissenberg, C. J. & MacLeod, C. J. (2016). A Reactive Porous Flow Control on Mid-ocean Ridge Magmatic Evolution. *Journal of Petrology* **57**, 2195–2220.

Lissenberg, C. J., MacLeod, C. J., Howard, K. A. & Godard, M. (2013). Pervasive reactive melt migration through fast-spreading lower oceanic crust (Hess Deep, equatorial Pacific Ocean). *Earth and Planetary Science Letters* **361**, 436–447.

Lissenberg, C.J., MacLeod, C.J. & Bennett, E.N. (2019). Consequences of a crystal mush-dominated magma plumbing system: a mid-ocean ridge perspective. *Philosophical Transactions of the Royal Society A* **377**(2139):.20180014.

Loocke, M. (2016). The role of the axial melt lens in crustal accretion at fast-spreading mid-ocean ridges. [PhD thesis, Cardiff University]. https://orca.cardiff.ac.uk/id/eprint/97663/

Martel, C., Pichavant, M., Holtz, F., Scaillet, B., Bourdier, J.-L. & Traineau, H. (1999). Effects of f O2 and H2O on andesite phase relations between 2 and 4 kbar. *Journal of Geophysical Research: Solid Earth* **104**, 29453–29470.

Marxer, F., Ulmer, P. & Müntener, O. (2022). Polybaric fractional crystallisation of arc magmas: an experimental study simulating trans-crustal magmatic systems. *Contributions to Mineralogy and Petrology* **177**, 3.

Marxer, F., Ulmer, P. & Müntener, O. (2023). Ascent-driven differentiation: a mechanism to keep arc magmas metaluminous? *Contributions to Mineralogy and Petrology* **178**, 51.

Melekhova, E., Blundy, J., Robertson, R. & Humphreys, M. C. S. (2015). Experimental Evidence for Polybaric Differentiation of Primitive Arc Basalt beneath St. Vincent, Lesser Antilles. *Journal of Petrology* **56**, 161–192.

Melekhova, E., Blundy, J., Martin, R., Arculus, R. & Pichavant, M. (2017). Petrological and experimental evidence for differentiation of water-rich magmas beneath St. Kitts, Lesser Antilles. *Contributions to Mineralogy and Petrology* **172**, 98.

Melekhova, E., Schlaphorst, D., Blundy, J., Kendall, J.-M., Connolly, C., McCarthy, A. & Arculus, R. (2019). Lateral variation in crustal structure along the Lesser Antilles arc from petrology of crustal xenoliths and seismic receiver functions. *Earth and Planetary Science Letters* **516**, 12–24.

Namur, O., Humphreys, M. C. S. & Holness, M. B. (2013). Lateral Reactive Infiltration in a Vertical Gabbroic Crystal Mush, Skaergaard Intrusion, East Greenland. *Journal of Petrology* **54**, 985–1016.

Nandedkar, R. H., Hürlimann, N., Ulmer, P. & Müntener, O. (2016). Amphibole–melt trace element partitioning of fractionating calc-alkaline magmas in the lower crust: an experimental study. *Contributions to Mineralogy and Petrology* **171**, 71.

Nixon, G. T., Manor, M. J., Scoates, J. S., Spence, D. W. & Milidragovic, D. (2024). Mineralogical constraints on magma storage conditions in ultramafic arc cumulates and the nature and role of cryptic fugitive melts: Tulameen Alaskan-type intrusion, North American Cordillera. *Contributions to Mineralogy and Petrology* **179**, 103.

Ortoleva, P., Merino, E., Moore, C. & Chadam, J. (1987). Geochemical self-organization I; reaction-transport feedbacks and modeling approach. *American Journal of Science* **287**, 979–1007.

Palme, H. & O’Neill, H. St. C. (2007). *2.01 - Cosmochemical Estimates of Mantle Composition*. In: Holland, H. D. & Turekian, K. K. (eds) *Treatise on Geochemistry*. Oxford: Pergamon, 1–38.

Paton, C., Hellstrom, J., Paul, B., Woodhead, J. & Hergt, J. (2011). Iolite: Freeware for the visualisation and processing of mass spectrometric data. *Journal of Analytical Atomic Spectrometry*. Royal Society of Chemistry **26**, 2508–2518.

Paulatto, M., Hooft, E. E. E., Chrapkiewicz, K., Heath, B., Toomey, D. R. & Morgan, J. V. (2022). Advances in seismic imaging of magma and crystal mush. *Frontiers in Earth Science*. Frontiers **10**.

Pichavant, M. & Macdonald, R. (2007). Crystallization of primitive basaltic magmas at crustal pressures and genesis of the calc-alkaline igneous suite: experimental evidence from St Vincent, Lesser Antilles arc. *Contributions to Mineralogy and Petrology*, **154**(5), 535-558.

Pichavant, M., Poussineau, S., Lesne, P., Solaro, C. & Bourdier, J.-L. (2018). Experimental Parametrization of Magma Mixing: Application to the ad 1530 Eruption of La Soufrière, Guadeloupe (Lesser Antilles). *Journal of Petrology* **59**, 257–282.

Plank, T. (2005). Constraints from Thorium/Lanthanum on Sediment Recycling at Subduction Zones and the Evolution of the Continents. *Journal of Petrology* **46**, 921–944.

Price, R. C., Smith, I. E. M., Stewart, R. B., Gamble, J. A., Gruender, K. & Maas, R. (2016). High-K andesite petrogenesis and crustal evolution: Evidence from mafic and ultramafic xenoliths, Egmont Volcano (Mt. Taranaki) and comparisons with Ruapehu Volcano, North Island, New Zealand. *Geochimica et Cosmochimica Acta* **185**, 328–357.

Putirka, K. D. (2008). Thermometers and Barometers for Volcanic Systems. *Reviews in Mineralogy and Geochemistry* **69**, 61–120.

Sanfilippo, A., MacLeod, C. J., Tribuzio, R., Lissenberg, C. J. & Zanetti, A. (2020). Early-Stage Melt-Rock Reaction in a Cooling Crystal Mush Beneath a Slow-Spreading Mid-Ocean Ridge (IODP Hole U1473A, Atlantis Bank, Southwest Indian Ridge). *Frontiers in Earth Science*. **8**, 579138.

Smith, D. J. (2014). Clinopyroxene precursors to amphibole sponge in arc crust. *Nature Communications* **5**, 4329.

Sparks, R. S. J., Annen, C., Blundy, J. D., Cashman, K. V., Rust, A. C. & Jackson, M. D. (2019). Formation and dynamics of magma reservoirs. *Philosophical Transactions of the Royal Society A: Mathematical, Physical and Engineering Sciences*. Royal Society **377**, 20180019.

Stamper, C. C., Blundy, J. D., Arculus, R. J. & Melekhova, E. (2014). Petrology of Plutonic Xenoliths and Volcanic Rocks from Grenada, Lesser Antilles. *Journal of Petrology* **55**, 1353–1387.

Streckeisen, A. (1976). To each plutonic rock its proper name. *Earth-Science Reviews* **12**, 1–33.

Tollan, P. M. E., Bindeman, I. & Blundy, J. D. (2012). Cumulate xenoliths from St. Vincent, Lesser Antilles Island Arc: a window into upper crustal differentiation of mantle-derived basalts. *Contributions to Mineralogy and Petrology* **163**, 189–208.

Turner, S. J. & Langmuir, C. H. (2015). The global chemical systematics of arc front stratovolcanoes: Evaluating the role of crustal processes. *Earth and Planetary Science Letters* **422**, 182–193.

Turner, S. J. & Langmuir, C. H. (2022). An Evaluation of Five Models of Arc Volcanism. *Journal of Petrology* **63**, egac010.

Villares, F., Blanco-Quintero, I. F., Reyes, P. S., Proenza, J. A., Cartagena, R., Lázaro, C. & Garcia-Casco, A. (2022). Petrogenesis of the Tampanchi Ultramafic–Mafic Complex (Ecuador): Geodynamic implications for the northwestern margin of South America during the late Cretaceous. *Gondwana Research* **105**, 514–534.

Wang, C., Liang, Y. & Xu, W. (2021). Formation of Amphibole-Bearing Peridotite and Amphibole-Bearing Pyroxenite Through Hydrous Melt-Peridotite Reaction and In Situ Crystallization: An Experimental Study. *Journal of Geophysical Research: Solid Earth* **126**, e2020JB019382.

Weber, G., Blundy, J., Barclay, J., Pyle, D. M., Cole, P., Frey, H., Manon, M., Davies, B. V. & Cashman, K. (2024). Petrology of the 2020–21 effusive to explosive eruption of La Soufrière Volcano, St Vincent: insights into plumbing system architecture and magma assembly mechanism. *Geological Society, London, Special Publications* **539**, 171–200.

Whitley, S., Halama, R., Gertisser, R., Hansteen, T. H., Frische, M. & Vennemann, T. (2024). A record of magmatic differentiation in plutonic xenoliths from Santorini (Greece). *Volcanica* **7**, 421–446.

Yang, A. Y., Wang, C., Liang, Y. & Lissenberg, C. J. (2019). Reaction Between Mid-Ocean Ridge Basalt and Lower Oceanic Crust: An Experimental Study. *Geochemistry, Geophysics, Geosystems* **20**, 4390–4407.

Zhang, W.-Q., Liu, C.-Z. & Dick, H. J. B. (2021). Evidence for Multi-stage Melt Transport in the Lower Ocean Crust: the Atlantis Bank Gabbroic Massif (IODP Hole U1473A, SW Indian Ridge). *Journal of Petrology* **61**, egaa082.

Figure captions

Figure 1: a) Olivine gabbro thin section (PPL) overview. Gap between images represents a small area of the thin section that was not imaged (~0.5 mm). **b)** Ol-Cpx gabbro thin section (PPL) overview. Red scale bar = 5 mm.

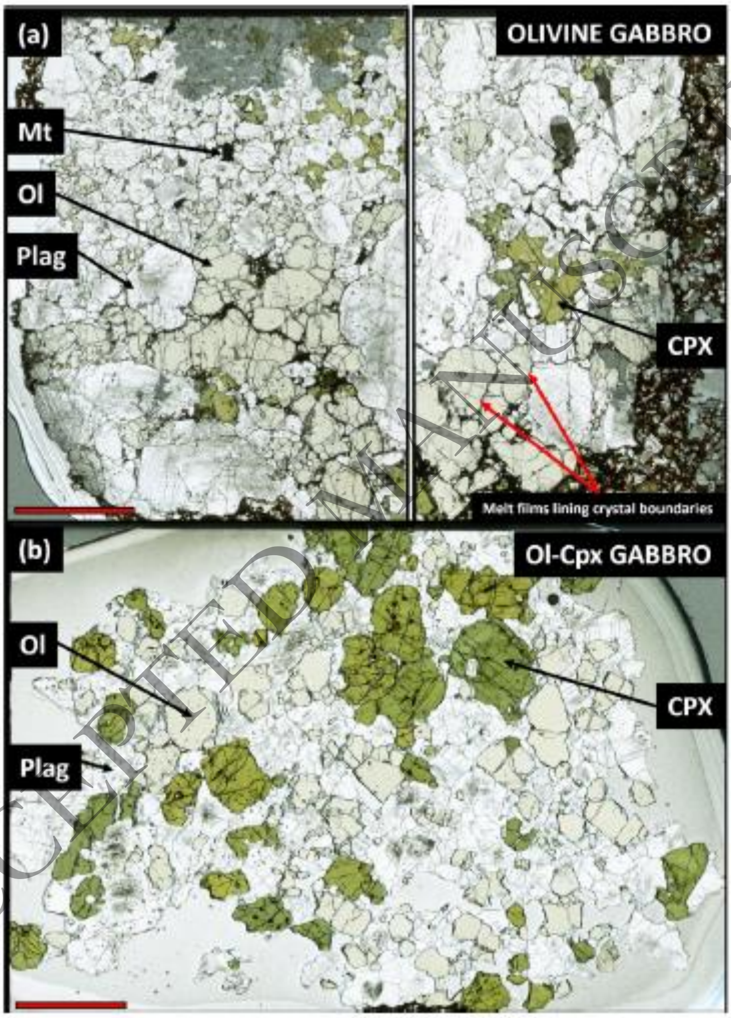

Figure 2: a) Banded gabbro thin section (PPL) overview with texturally distinct "plag-cpx band" labelled (boundary marked by red dashed line). The remainder of the sample is referred to as the sample "matrix". Red scale bar = 5 mm. **b)** and **c)** PPL images of amphibole (brown) overgrowths on the rims of clinopyroxene (pale green) from banded gabbro matrix. **d)** PPL image of plagioclase and clinopyroxene within the "plag-cpx band", highlighting the melt and fluid inclusion rich plagioclase. **e)** PPL image of the boundary between the banded gabbro matrix and "plag-cpx band" (red dashed line). White scale bars = 1 mm.

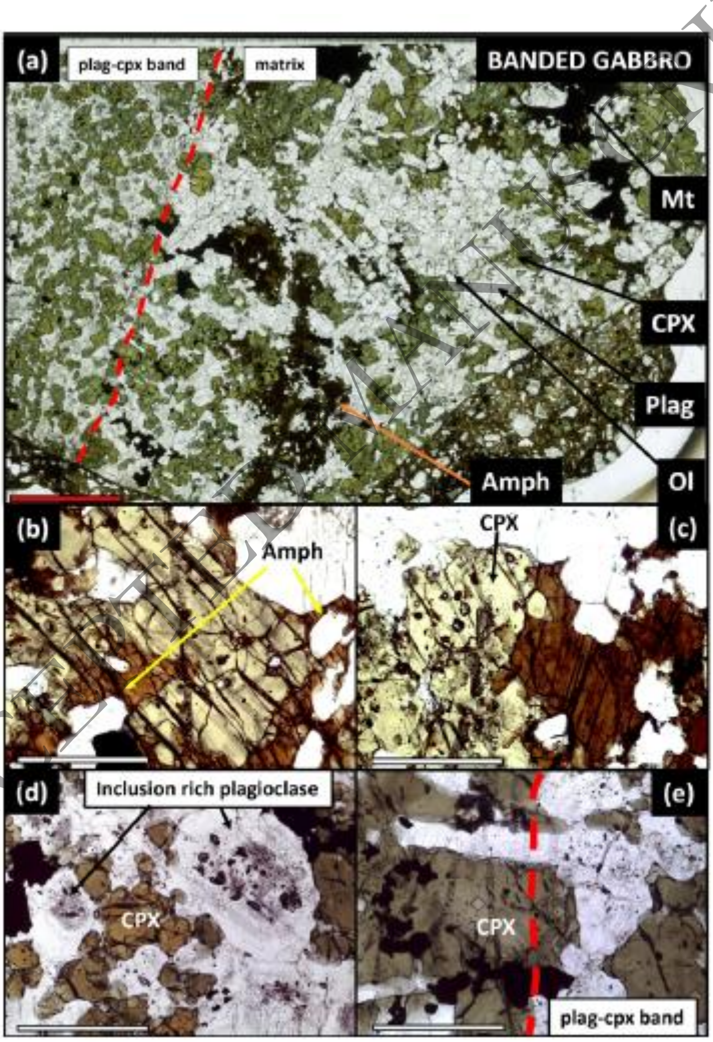

Figure 3: **a)** Poikilitic gabbro thin section (PPL) overview. Red scale bar = 5 mm. **b)** PPL image of zoned clinopyroxene (CPX) with poikilitic amphibole (Amph) replacing rim. Note the ragged contact between clinopyroxene and amphibole. **c)** XPL image showing example of poikilitic orthopyroxene (OPX) surrounding embayed olivine (OL). **d)** PPL image of poikilitic amphibole surrounding both clinopyroxene and embayed olivine. **e)** XPL image of zoned plagioclase (PLAG) with relict core outlined (yellow dashes). Correspondence with the chemical map shows that this core has a high An content. The shape of the relict core is suggestive of resorption. Note the clinopyroxene inclusions in the crystal zone outside the relict core. White scale bars = 1 mm.

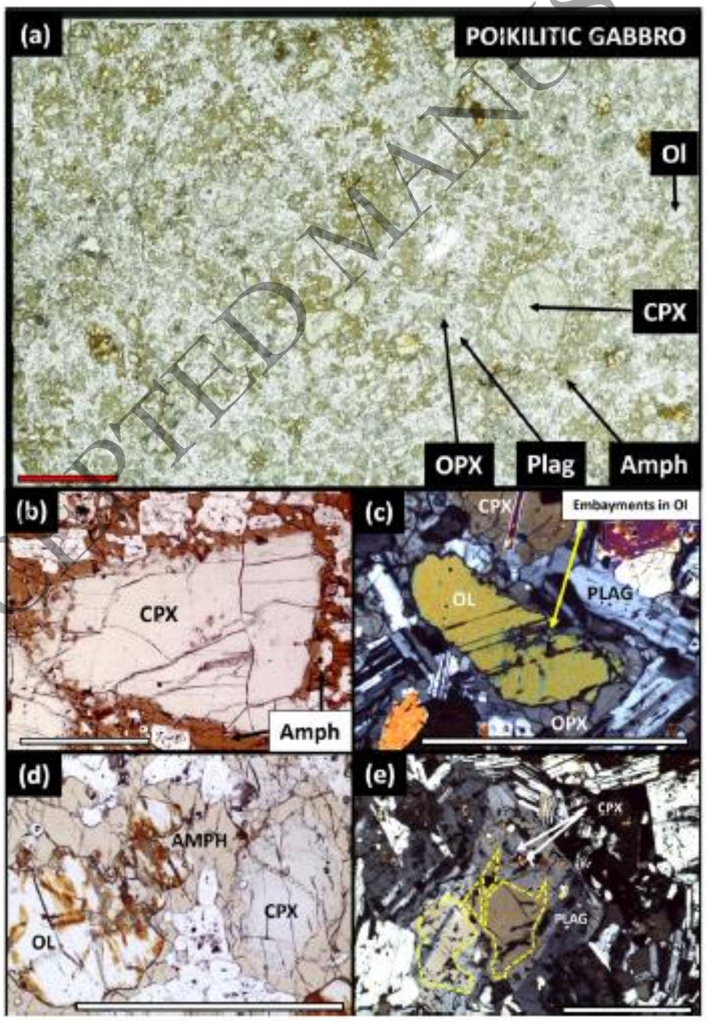

Figure 4: a) Quantitative Mg# in clinopyroxene and **b)** quantitative An in plagioclase thin section maps for banded gabbro. The dashed lines highlight the texturally distinct, “plag-cpx band”. The QUACK software used to generate the maps outputs the Mg# and An values, shown on the right of the maps, as decimals, e.g. An_{90} = 0.9, Mg# 80 = 0.8. **c)** Zoomed in clinopyroxene Mg# map across the contact between the “plag-cpx band” and “matrix”.

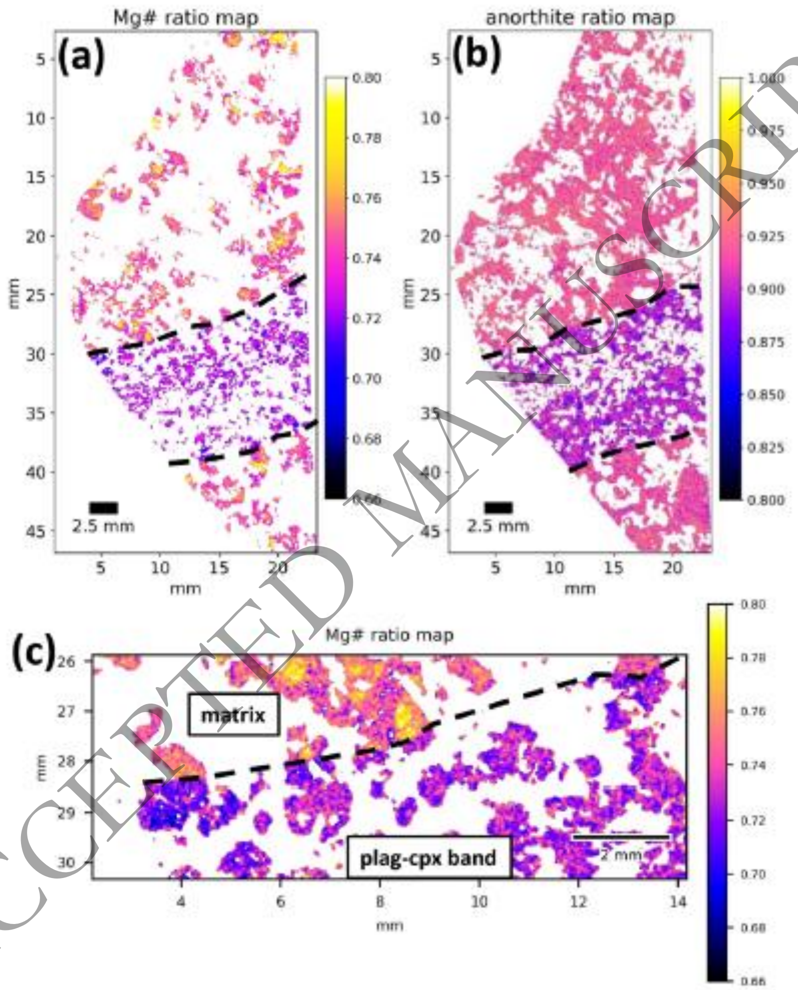

Figure 5: a) Quantitative Mg# in clinopyroxene and **b)** quantitative An in plagioclase thin section maps for poikilitic gabbro. The QUACK software used to generate the maps outputs the Mg# and An values, shown on the right of the maps, as decimals, e.g. An_{90} = 0.9, Mg# 80 = 0.8.

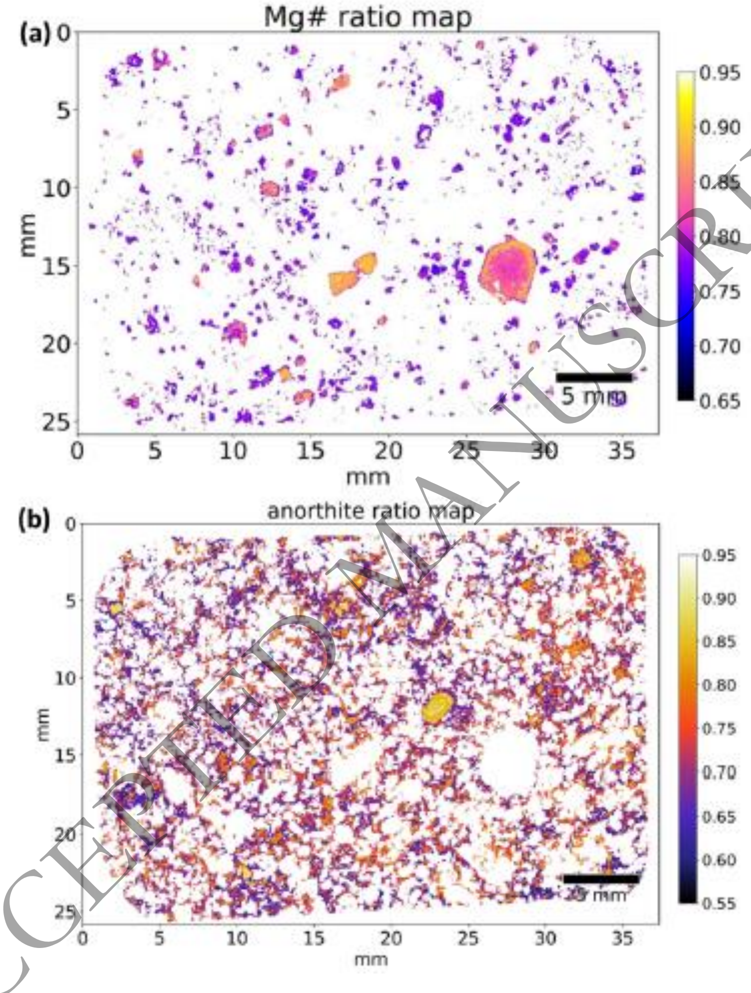

Figure 6: a) Zr **b)** Y **c)** Ce **d)** Cr **e)** Ni vs Mg#, and **f)** La vs Yb, for clinopyroxene from the plutonic xenolith samples. Black bar with circle shows 2SD % uncertainty. Error bars on individual data points show internal 2SE uncertainty. Where error bars are not visible, uncertainty is smaller than symbol size. Uncertainty on Mg# values is inferred to be < 1 % (see methods).

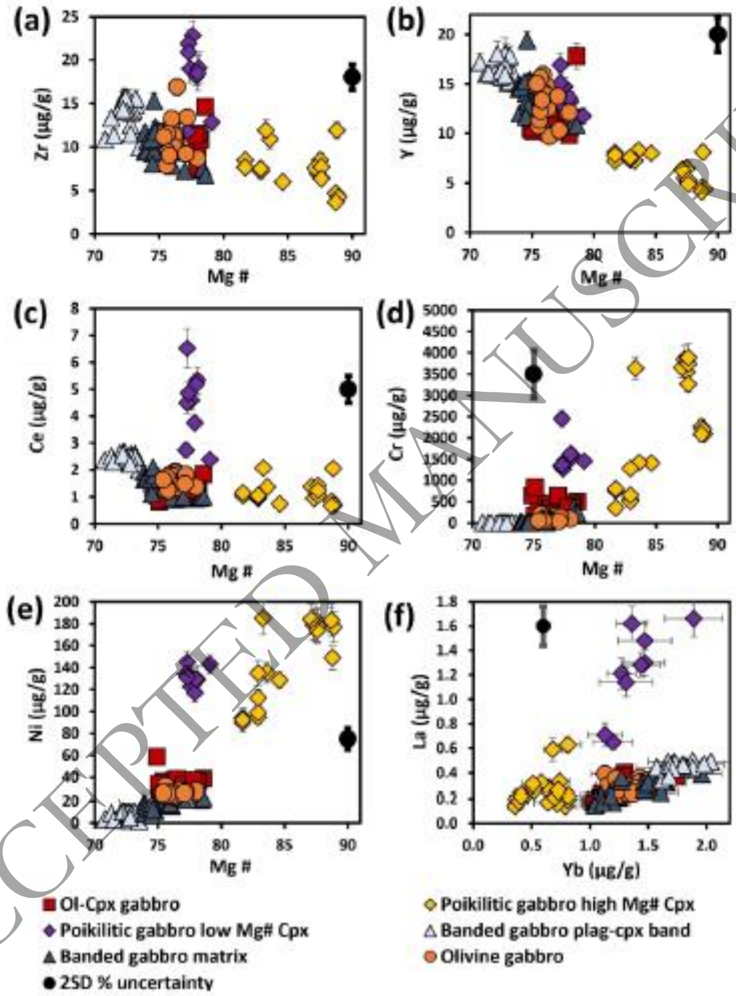

Figure 7: Primitive mantle (Palme and O'Neill, 2003) normalized REE patterns for clinopyroxene from **a)** poikilitic gabbro **b)** banded gabbro **c)** olivine gabbro **d)** Ol-Cpx gabbro. For comparison, the compositional range of high Mg# clinopyroxene from the poikilitic gabbro are shown (yellow shaded area) on panels b), c) and d).

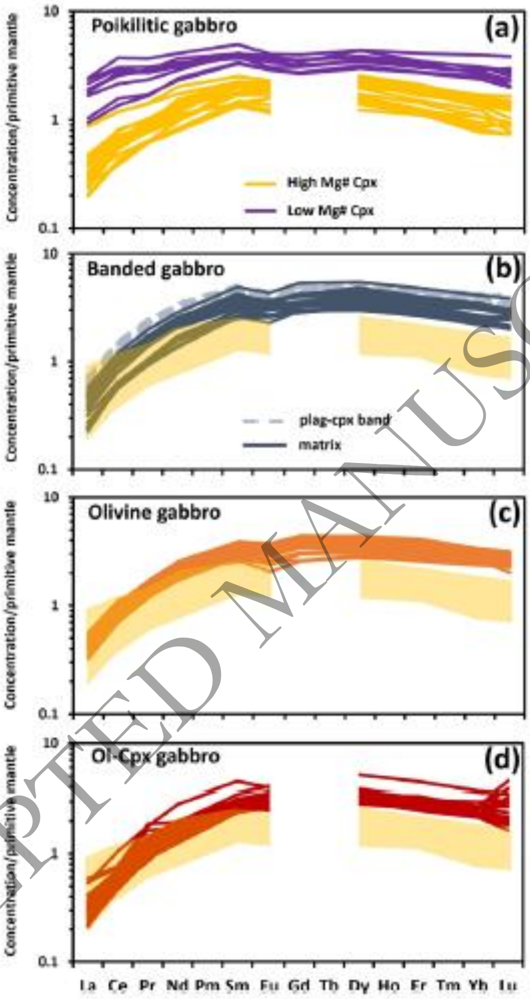

Figure 8: a) Zr vs Y **b)** Ba vs Nb **c)** Cr vs Ni for banded and poikilitic gabbro amphibole. Black bars with circle show 2SD % uncertainty. Error bars on individual data points show internal 2SE uncertainty. Where error bars are not visible, uncertainty is smaller than symbol size. **d)** Primitive mantle normalized REE patterns for banded and poikilitic gabbro amphibole. Shown for comparison are amphibole compositions from Martinique plutonic xenoliths with different textural characteristics ("MQ" in legend, labelled shaded fields). NCG = non-cumulate gabbro. Martinique plutonic xenolith amphibole data from Cooper *et al*., (2016). Primitive mantle normalizing values from Palme and O'Neill (2003).

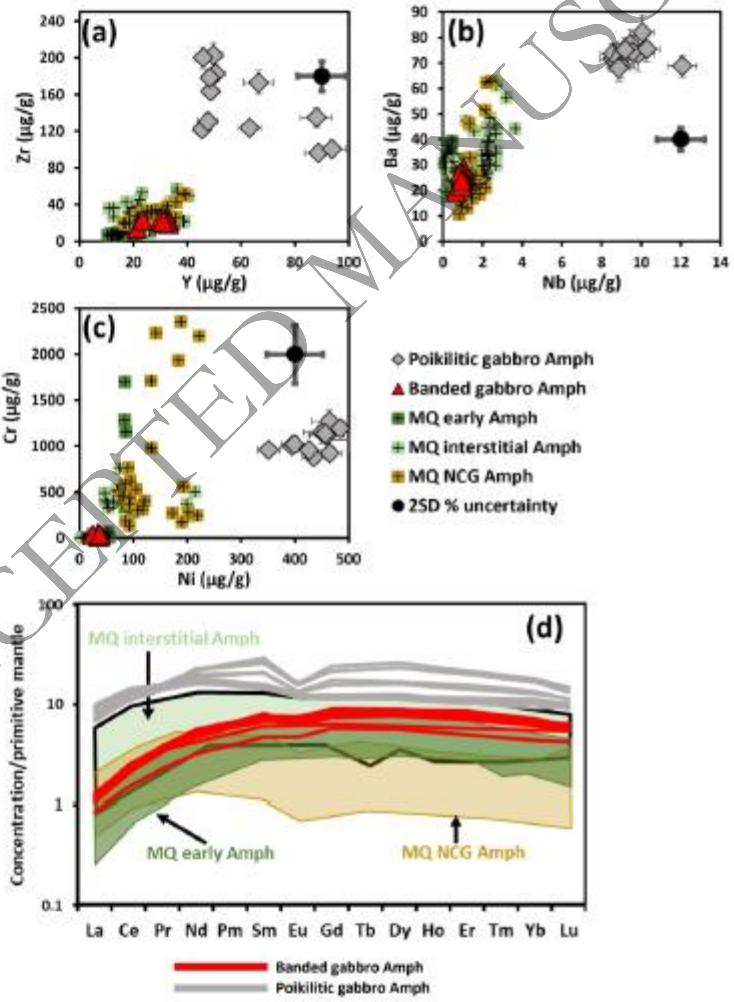

Figure 9: a) Ce **b)** Nd **c)** Sm **d)** Dy vs Yb for clinopyroxene from the Ol-Cpx gabbro, olivine gabbro and banded gabbro matrix, compared with the clinopyroxene composition in equilibrium with the melt in models FC1 and FC2. The modelled clinopyroxene compositions were calculated from modelled melt compositions using partition coefficients at 49 wt % SiO_2 (Supplementary Table ST5). Error bars on individual data points show internal 2SE uncertainty. The FC1 and FC2 models are shown as symbols (diamond, cross), with each symbol representing an increment of 10 % crystallisation (abbreviated to xtln). The symbols marked “50 % xtln” represent the clinopyroxene composition in equilibrium with the melt after 50 % crystallisation. The coloured stars indicate the composition of clinopyroxene in equilibrium with the initial melt composition used for models FC1 and FC2.

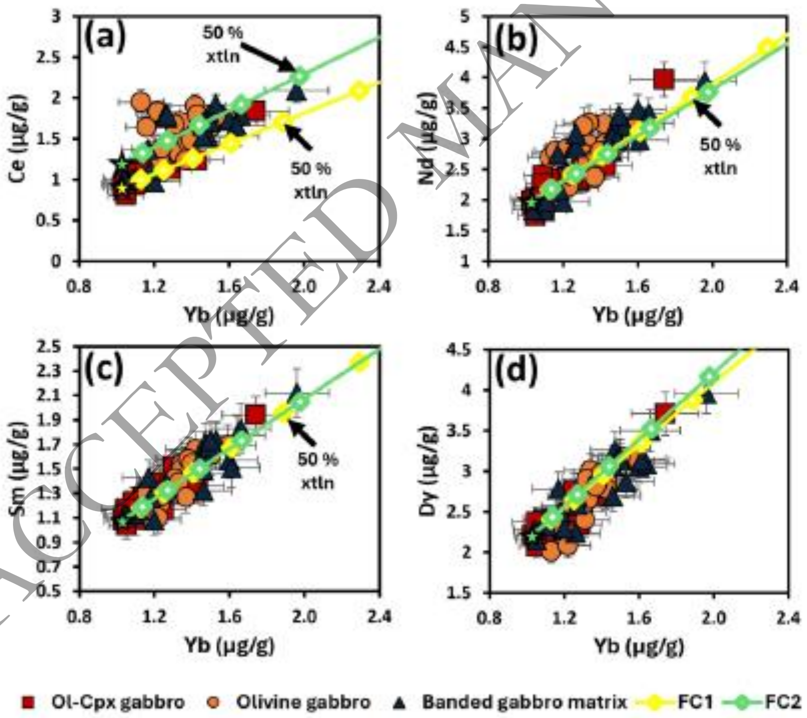

Figure 10: a) Ce **b)** Nd **c)** Sm **d)** Dy vs Yb for clinopyroxene from the plag-cpx band, compared with the clinopyroxene composition in equilibrium with the melt in model AFC2. The modelled clinopyroxene compositions were calculated from modelled melt compositions using partition coefficients at 49 wt % SiO_2 (Supplementary Table ST5). Error bars on individual data points show internal 2SE uncertainty. Each circle on AFC model curves represents an increment of 10 % crystallisation (abbreviated to xtln). The coloured star indicates the composition of clinopyroxene in equilibrium with the initial melt composition used for model AFC2.

e) Primitive mantle normalised REE compositions of banded gabbro amphibole (red) compared with the composition of amphibole in equilibrium with the melt after 60-70% crystallisation (abbreviated to xtln) in model FC2. The modelled amphibole compositions were calculated from modelled melt compositions using partition coefficients at 53 wt % SiO_2 (Supplementary Table ST5). Primitive mantle normalizing values from Palme and O'Neill (2003).

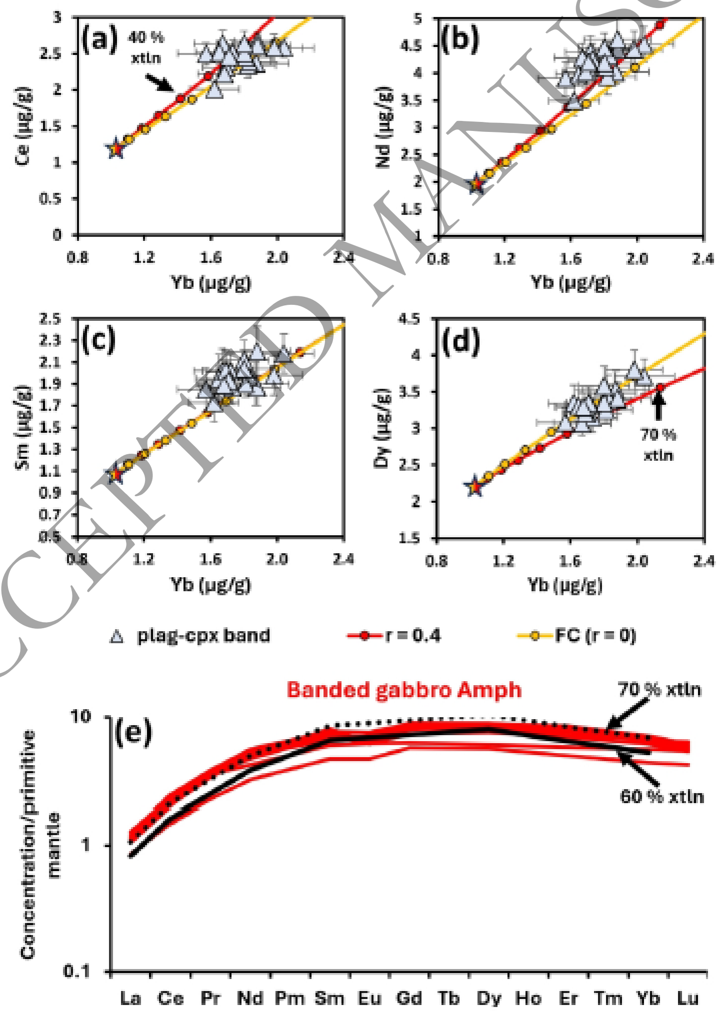

Figure 11: a) Ce **b)** Nd **c)** Sm **d)** Dy vs Yb for the poikilitic gabbro low Mg# clinopyroxene compared with the clinopyroxene composition in equilibrium with the melt in models FC3 and AFC1 (r = 0.4, 0.55, 0.8). The modelled clinopyroxene compositions were calculated from modelled melt compositions using partition coefficients at 59 wt % SiO_2 (Supplementary Table ST5). The range of r values shown for the AFC model represent upper and lower bounds which encompass the sample data. Error bars on individual data points show internal 2SE uncertainty. Each circle on AFC and FC model curves represents an increment of 10 % crystallisation (abbreviated to xtln). The coloured stars indicate the composition of clinopyroxene in equilibrium with the initial melt composition used for models FC3 and AFC1.

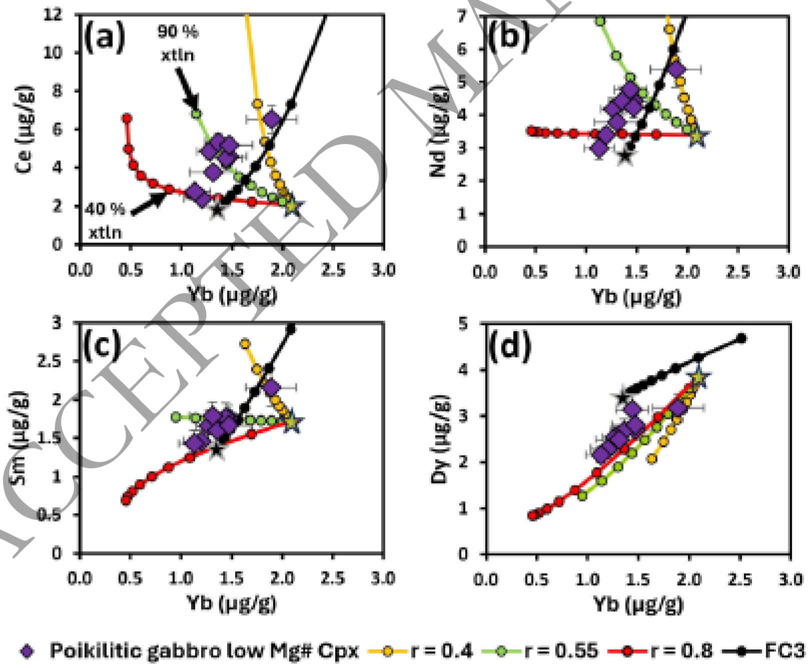

Figure 12: a) Ce **b)** Nd **c)** Sm **d)** Dy vs Yb for the poikilitic gabbro amphibole compared with the amphibole composition in equilibrium with the melt in models FC3 and AFC1 (r = 0.15, 0.3, 0.4). The modelled amphibole compositions were calculated from modelled melt compositions using partition coefficients at 59 wt % SiO_2 (Supplementary Table ST5). The range of r values shown for the AFC model represent upper and lower bounds which encompass the sample data. Error bars on individual data points show internal 2SE uncertainty. Each circle on AFC and FC model curves represents an increment of 10 % crystallisation (abbreviated to xtln). The coloured stars indicate the composition of amphibole in equilibrium with the initial melt composition used for models FC3 and AFC1.

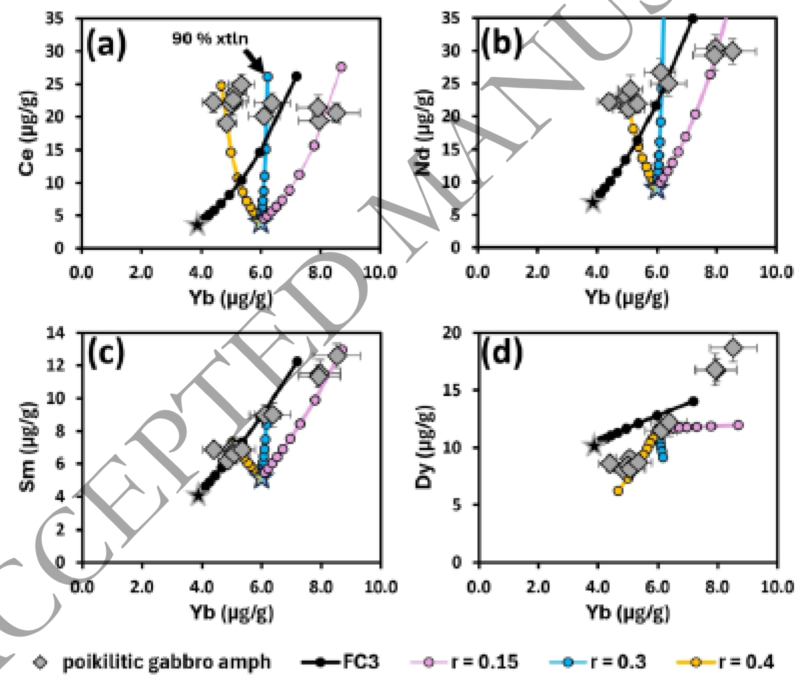

Figure 13: Stage 1 – An evolved, hydrous reactive melt infiltrates an initial mush composed of high An plagioclase, olivine and high Mg# Cpx.

Stage 2 – Chemical disequilibrium between the invading melt and initial mush triggers reactions which leads to partial dissolution of the high An plagioclase, olivine and the high Mg# Cpx. The reactions crystallise poikilitic orthopyroxene around partially dissolved olivine and poikilitic amphibole around olivine and the high Mg# Cpx. Plagioclase An$_{75-85}$ and the low Mg# Cpx population also crystallise from the melt, which has been chemically modified by reaction with the mush. A new plagioclase-orthopyroxene-clinopyroxene-amphibole mush (with remnant An$_{85-90}$ plagioclase, olivine and high Mg# Cpx) is formed.

Stage 3 – Late-stage crystallisation of residual evolved melts in the mush formed low An$_{60-75}$ plagioclase, additional amphibole overgrowths and apatite.

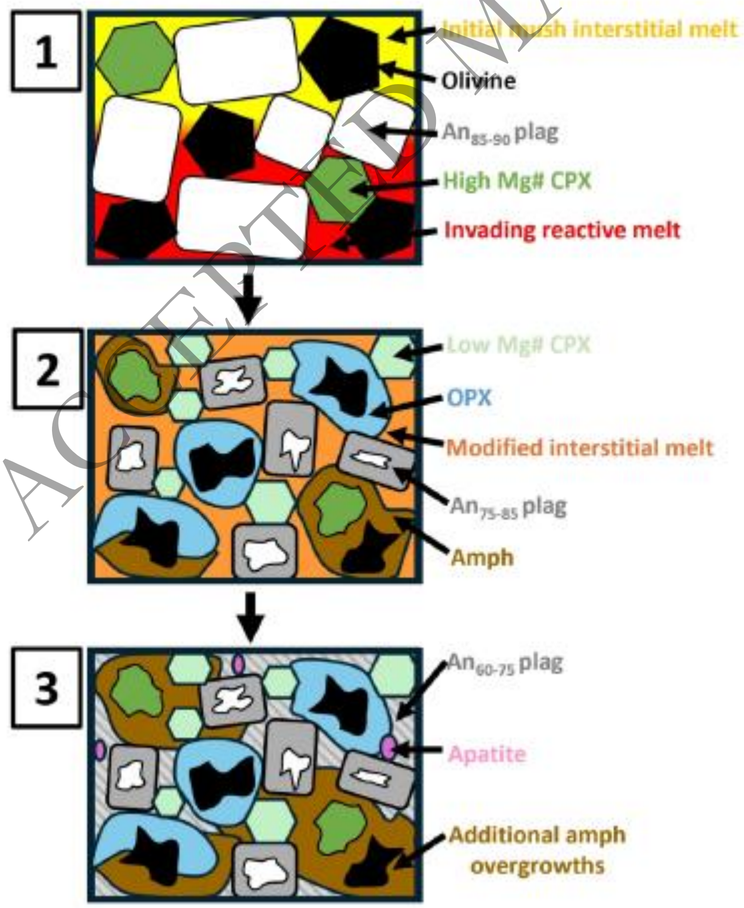

Figure 14: Schematic illustrating possible "reactive infiltration feedback" scenario for formation of the plag-cpx band in the banded gabbro**.** A small region of higher porosity was present in the initial olivine gabbro mush, allowing a greater flux of reactive melt, causing faster dissolution in this region. Subsequently, new plagioclase and clinopyroxene precipitated from the reactive melt in the channel formed via preferential dissolution, forming the plag-cpx band.

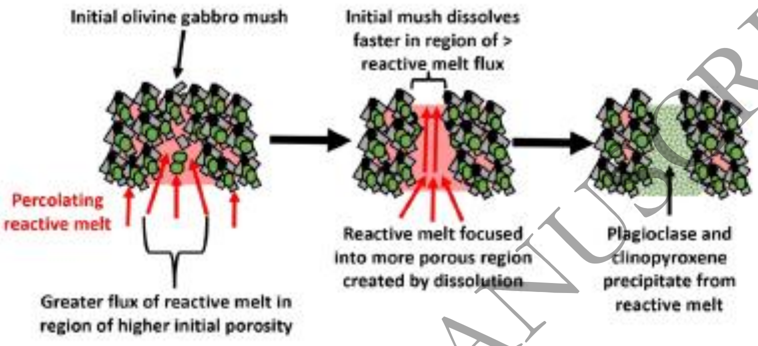

Figure 15: REE compositions of melts in equilibrium with banded gabbro “plag-cpx band” clinopyroxene, poikilitic gabbro low Mg# clinopyroxene and amphibole. The equilibrium melt compositions were calculated using the following partition coefficients: banded gabbro clinopyroxene – 49 wt % SiO_2, poikilitic gabbro low Mg# clinopyroxene and amphibole - 59 wt % SiO_2 (Supplementary Table ST5). Equilibrium melt compositions are compared with whole-rock data for St Vincent lavas (Heath *et al*., 1998; Plank, 2005; DuFrane *et al*., 2009; Fedele *et al*., 2021) and melt inclusions (MI’s) (Bouvier *et al*., 2010, 2022; Cooper *et al*., 2020; Balcone-Boissard *et al*., 2023).

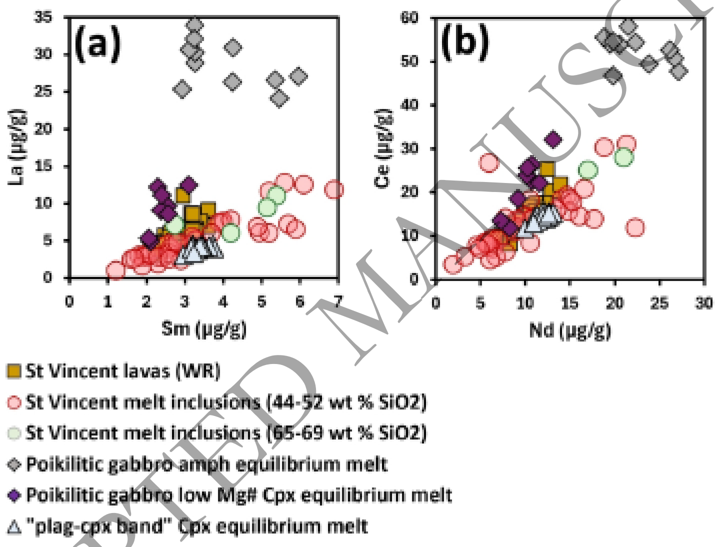

Table 1: Key petrographic and chemical characteristics of the four plutonic xenoliths analysed for mineral trace element compositions in this study. The proportions of mineral phases were determined from thin section chemical maps using the python GUI program "QUACK" (Loocke, 2016). Crystallisation depths were estimated through comparison of plutonic xenolith mineral assemblages and compositions with the products of crystallisation experiments (Supplementary Table ST4).

Sample name and sampling location (latitude, longitude)	Mineral assemblage and proportions	Plag An	Ol Fo	Cpx Mg#	Opx Mg#	Amp Mg#	Key textural features	Textures support melt-mush reaction?	Estimated crystallisation depth (km)
Olivine gabbro (13˚ 17' 52.7", 61˚ 07' 05.7")	Plag (69 %), Ol (22 %), Cpx (8 %), Mt (1 %)	89-98	76-79	70-80			-Primocryst Plag and Ol, interstitial Cpx and Mt. -Interstitial melt films line most crystal boundaries	No	6-18
Ol-Cpx gabbro (13˚ 17' 52.7", 61˚ 07' 05.7")	Plag (52 %), Ol (23 %), Cpx (25 %)	90-100	77-80	72-81			-Primocryst Plag, Ol, Cpx. -Well equilibrated 120° contacts between primocryst phases common	No	6-18
banded gabbro (13˚ 19' 37.3", 61˚ 10' 17.6")	Plag (58 %), Ol (2 %), Cpx (29 %), Mt (4 %), Amph (7 %)	85-97	72-76	69-80		62-70	-Sample "matrix" contains Ol, Plag, Cpx primocrysts with interstitial Amph and Mt -Interstitial Amph found overgrowing rims of Cpx in matrix. -"plag-cpx band" cross-cuts matrix, defined by smaller crystal size, inclusion rich plagioclase and absence of olivine.	Yes – "plag-cpx band" with distinctive mineralogy and chemistry compared with matrix.	~12
poikilitic gabbro (13˚ 15' 11.0", 61˚ 07' 06.1")	Plag (53 %), Ol (8 %), Cpx (12 %), Opx (12 %), Amph (15 %) (plus minor accessory oxides, apatite and sulfides)	60-90	70-76	70-90	72-75	65-70	-2 Cpx size populations (> 1 mm euhedral, < 1 mm subhedral). -Poikilitic amph replaces embayed rims of Cpx and Ol, poikilitic Opx replaces embayed Ol rims -Zoned plagioclase with relict high-An cores	Yes – relict high An plagioclase cores, poikilitic Amph and Opx replacing embayed Ol and Cpx rims	High Mg# Cpx – 12 or 30, other mineral phases ~5-12